

**Probing the Local Structure of Pure Ionic Liquid Salts with ^{35}Cl , ^{79}Br and ^{127}I Solid
State NMR**

by Peter George Gordon, B.Sc.

A thesis submitted to the Faculty of Graduate Studies and Research

in partial fulfillment of the requirements for the degree of

Master of Science

to

The Faculty of Graduate Studies and Research

Department of Chemistry

Carleton University

Ottawa, Ontario

Canada



Library and
Archives Canada

Published Heritage
Branch

395 Wellington Street
Ottawa ON K1A 0N4
Canada

Bibliothèque et
Archives Canada

Direction du
Patrimoine de l'édition

395, rue Wellington
Ottawa ON K1A 0N4
Canada

Your file *Votre référence*
ISBN: 978-0-494-44123-7
Our file *Notre référence*
ISBN: 978-0-494-44123-7

NOTICE:

The author has granted a non-exclusive license allowing Library and Archives Canada to reproduce, publish, archive, preserve, conserve, communicate to the public by telecommunication or on the Internet, loan, distribute and sell theses worldwide, for commercial or non-commercial purposes, in microform, paper, electronic and/or any other formats.

The author retains copyright ownership and moral rights in this thesis. Neither the thesis nor substantial extracts from it may be printed or otherwise reproduced without the author's permission.

AVIS:

L'auteur a accordé une licence non exclusive permettant à la Bibliothèque et Archives Canada de reproduire, publier, archiver, sauvegarder, conserver, transmettre au public par télécommunication ou par l'Internet, prêter, distribuer et vendre des thèses partout dans le monde, à des fins commerciales ou autres, sur support microforme, papier, électronique et/ou autres formats.

L'auteur conserve la propriété du droit d'auteur et des droits moraux qui protègent cette thèse. Ni la thèse ni des extraits substantiels de celle-ci ne doivent être imprimés ou autrement reproduits sans son autorisation.

In compliance with the Canadian Privacy Act some supporting forms may have been removed from this thesis.

Conformément à la loi canadienne sur la protection de la vie privée, quelques formulaires secondaires ont été enlevés de cette thèse.

While these forms may be included in the document page count, their removal does not represent any loss of content from the thesis.

Bien que ces formulaires aient inclus dans la pagination, il n'y aura aucun contenu manquant.

■ ■ ■
Canada

Abstract

Room Temperature Ionic Liquids (RTILs) are considered part of the green chemistry paradigm due to their negligible vapour pressure and ease of recycling. Evidence of liquid state order, observed by IR and Raman spectroscopy, diffraction studies, and simulated by ab initio methods, has been reported in the literature. Here, quadrupolar nuclei are used as NMR probes to extract information about the solid and possible order in the liquid state of RTILs. The anisotropic nature and field dependence of quadrupolar and chemical shift interactions are exploited to this end. Relaxation time measurements are employed to investigate the molecular motions present in the liquid state and infer what kind of order is present. The results obtained indicate that on the timescale of the NMR experiment ($\sim 10^{-8}$ sec), RTILs behave as isotropic liquids with no residual order.

Acknowledgements

Firstly I would like to express my gratitude to John Ripmeester and Darren Brouwer. John provided me with the opportunity to pursue my Master's studies and rediscover my love of learning and research; his support and advice has been invaluable. Darren's unlimited patience, talent for explaining complex concepts, and enthusiasm has been instrumental to my development as a researcher. I have them to thank for a great experience at the National Research Council and for the skills and confidence to pursue my Doctorate degree.

Working with the SIMS group has been a fascinating experience, and I thank you all for your help and advice. Being surrounded by knowledgeable, supportive people is a rare and wonderful thing. In particular I would like to thank Steve Lang, Igor Moudrakovski, Victor Terskikh, Jamie Bennett, Chris Ratcliffe and Gary Enright.

I would also like to thank Seán Barry and the Barry Lab. Seán took a chance on me when he brought me into his group for my qualifying year. Working with him and his group convinced me that I had made the right choice in coming back to school.

Finally I would like to thank my friends and family for their unconditional support. I am of course particularly and absolutely thankful for the unwavering support of my parents Sue Smarkala and Don Gordon, and their loving partners Joe Smarkala and Nancy Gordon. Without them none of this would be possible.

Table of Contents

	Page
Title Page.....	i
Abstract.....	ii
Acknowledgements.....	iii
Table of Contents.....	iv
List of Tables.....	vi
List of Figures.....	vii
List of Appendices.....	ix
Chapter 1: Introduction.....	1
1.1 Ionic Liquids: Definitions, History and Current Research.....	1
1.2 Nuclear Magnetic Resonance Spectroscopy.....	4
Chapter 2: Solid State Quadrupolar NMR.....	10
2.1 The Quadrupolar Interaction.....	14
2.2 Shielding and Chemical Shift.....	18
2.3 Quadrupolar NMR techniques.....	21
2.3.1 Magic Angle Spinning.....	22
2.3.2 Hahn Echo and Solid Echo Pulse Programs.....	25
2.3.3 Proton Decoupling.....	27
2.3.5 T ₁ and T ₂ Relaxation.....	27
2.4 Simulations and Computational Methods.....	34
2.4.1 DMfit.....	34
2.4.2 Bruker Topspin.....	34
2.4.3 Gaussian 98.....	34
Chapter 3: RTIL Solid- and Liquid-state Structure.....	36
3.1 Solution NMR.....	37
3.2 Computer Simulation.....	38
3.3 Neutron Diffraction.....	39
3.4 X-ray diffraction.....	41
3.5 Raman and FTIR Spectroscopy.....	43
Chapter 4: Results and Discussion of IL Characterization.....	46
4.1 Differential Scanning Calorimetry.....	46
4.2 NMR Spectroscopy.....	50
4.2.1 Solid State NMR Results.....	51
4.2.2 Liquid State NMR Results.....	56
4.2.3 Gaussian Calculations.....	64
Chapter 5: Conclusions.....	66
Chapter 6: Experimental Details.....	67
6.1 Preparation of Samples.....	67
6.1.1 Reference Samples.....	67
6.1.2 Ionic Liquid Samples.....	68
6.2 Solid and Liquid State NMR.....	69
6.2.1 NMR Spectrometers and Probes.....	69
6.2.2 Magic Angle Spinning (MAS).....	70
6.2.3 Variable Temperature NMR (VTNMR).....	70
6.3 Computer simulation.....	71

6.3	Differential Scanning Calorimetry	73
	Chapter 7: References	74
	Chapter 8: Appendices	78
8.1	NMR pulse sequence programs	78
8.2	Relaxation Time Experimental Data	82
8.3	NMR Acquisition Parameters	83
8.4	Gaussian 98 Input Files	85

List of Tables

	page
Table 1 Melting points of studied ILs in °C	50
Table 2 ³⁵ Cl experimental spectrum simulation fit parameters. Labelled parameters correspond to their respective numbered peaks in Figure 24	52
Table 3 ⁷⁹ Br experimental spectrum simulation fit parameters.	55
Table 4 ¹²⁷ I experimental spectrum simulation fit parameters.....	56
Table 5 ³⁵ Cl nuclear quadrupole and CSA parameters calculated by Gaussian 98 (G98), and experimental data. Monoclinic bmim values marked by *; not observed experimentally.....	64
Table 6 Cations, their structures and abbreviations. Also shown are the anion pairs for a given cation investigated in this work.	68
Table 7 ³⁵ Cl SSNMR MAS acquisition parameters (21.15 T).....	83
Table 8 ³⁵ Cl SSNMR static acquisition parameters.....	83
Table 9 ³⁵ Cl liquid NMR acquisition parameters	84
Table 10 ⁷⁹ Br SSNMR static acquisition parameters.....	84
Table 11 ⁷⁹ Br liquid NMR acquisition parameters	84
Table 12 ¹²⁷ I SSNMR static acquisition paramters.....	84
Table 13 ¹²⁷ I SSNMR MAS acquisition parameters.....	84

List of Figures

	page
Figure 1 Numbering scheme for imidazolium rings	2
Figure 2 Cations studied in this work and their abbreviations.....	3
Figure 3 Decomposition of a) field oscillating along the x-axis into b) two fields rotating in opposite directions.	6
Figure 4 Stationary laboratory frame (x,y,z) and rotating frame (x',y',z')	7
Figure 5 Precession of the spin ensemble magnetization about B_{1x} in the rotating frame by a) 90° and b) 180°	8
Figure 6 Spin 3/2 nuclei spin energy levels with and without an applied magnetic field. In the absence of a field, the m spin states are degenerate.	11
Figure 7 First- and second-order quadrupolar interaction effects on a spin-5/2 nucleus. 12	
Figure 8 Quadrupolar spectra arising from a) small CQ and b) large CQ.....	13
Figure 9 Sensitivity of spectra to C_Q and η_Q (credit: R.W. Schurko ¹).....	17
Figure 10 Determining CSA parameters from a spectrum	19
Figure 11 Examples of symmetry of the chemical shift tensor and the resulting CSA powder patterns; a) spherical, b) non-axial (shielding is different in all three directions) and c) axial.....	20
Figure 12 Describing the relative orientation of two axis systems, beginning with a) aligned axes then b) rotating about the z-axis by α , c) rotating about y' by β and finally d) rotating about z' by γ	21
Figure 13 Origin of the CSA powder pattern.....	23
Figure 14 MAS experimental set-up, where B_0 is the applied magnetic field and the sample rotor is rotated about an axis oriented at an angle of 54.74° to the field.....	23
Figure 15 Hahn Echo pulse sequence	26
Figure 16: (A) Half-echo 127I FID. (B) Whole-echo 127I FID. (C) The direct FT of the whole-echo FID shown in (B). (D) FT followed by first-order phase correction of the whole-echo FID shown in (B). The sample is NaIO_4 ²	26
Figure 17 Inversion-recovery pulse sequence and FID. Acquisition begins after $\pi/2$ pulse.	29
Figure 18 The inversion-recovery experiment. Peak intensity is plotted against time delay τ	30
Figure 19 Hahn echo pulse sequence and resulting FID. Signal acquisition begins after π pulse.	31
Figure 20 Schematic illustration of the dependence of relaxation times on temperature 33	
Figure 21 Raman spectra of the bmim[Cl] polymorphs and supercooled liquid.....	43
Figure 22 FTIL spectra of solid and liquid emim[Cl].....	44
Figure 23 DSC plots for chloride ILs. Ramp rate = $2^\circ\text{C}/\text{min}$ for a)-c), $1^\circ\text{C}/\text{min}$ for d). All samples were heated from room temperature, and held at 10-minute isotherms before changing temperature ramp direction	48
Figure 24 DSC plots for (a) bromide and (b),(c),(d) iodide ILs. Ramp rate = $1^\circ\text{C}/\text{min}$ for (a) and (b), $5^\circ\text{C}/\text{min}$ for (c) and (d). All samples were heated from room temperature, and held at 10-minute isotherms before changing temperature ramp direction	49
Figure 25 Experimental (solid lines) and simulated (dashed lines) SSNMR ^{35}Cl spectra.	52

Figure 26 Experimental (solid lines) and simulated (dashed lines) SSNMR ^{79}Br spectra.	54
Figure 27 Experimental (solid lines) and simulated (dashed lines) SSNMR ^{127}I spectra.	55
Figure 28 Liquid-state ^{35}Cl spectra for a) emim, b) bmim and c) bdmim chlorides at 9.4 T (upper) and 4.7 T (lower).	57
Figure 29 DSC profile with NMR spectra at 9.4 T for emim[Cl].....	58
Figure 30 DSC profile with NMR spectra at 9.4 T for bmim[Cl]	58
Figure 31 DSC profile with NMR spectra at 9.4 T for bdmim[Cl]	59
Figure 32 ^{35}Cl VTNMR at 9.4 T of bmim[Cl], cooled from 80°C to 50°C	60
Figure 33 Liquid-state ^{79}Br spectra for a) emim and b) bmim bromides at 9.4 T (upper) and 4.7 T (lower).....	61
Figure 34 Relaxation times for a) emim, b) bmim and c) bdmim chlorides. Closed squares represent T_1 values and open squares represent T_2 values.....	63
Figure 35 Relaxation times for a) emim and b) bmim bromides. Closed squares represent T_1 values and open squares T_2 values.	63
Figure 36 Comparison of parameters calculated with Gaussian 98 and experimental data. Dashed line represents best-case scenario of Calculated = Experimental. The equation for the line of best fit (solid line in right chart) is $y = 1.5616x - 48.428$, with an R-value of 0.8659.....	65

List of Appendices

8.1 NMR Pulse sequence programs	
zg; single pulse.....	90
zg; single pulse with high-power proton decoupling.....	90
90/180 echo.....	91
90/180 echo with high power proton decoupling.....	92
T1 experiments: t1ir.....	93
T2 experiments: t2_hahn.....	93
8.2 Relaxation Time Experimental Data.....	94
8.3 NMR Acquisition Parameters.....	96
8.4 Gaussian 98 Input Files	
Rough proton optimization.....	97
Refined proton optimization.....	98
EFG calculation.....	98
Shielding calculation.....	99

Chapter 1: Introduction

1.1 Ionic Liquids: Definitions, History and Current Research

Ionic liquids (ILs) have been known for nearly a century³ but initially there was little interest in investigating their use as solvents. Organic chloroaluminates, first mentioned in 1951 but only studied in detail beginning in the 1970s are considered to form the first generation of ILs⁴. These early ILs were subject to rapid hydrolysis, requiring an inert atmosphere for handling, forming a barrier to development. Air- and water-stable ILs were developed in the 90s and subsequently they have garnered increasing interest due to both the ease of use of this new generation of materials and their unique characteristics.

In contrast to the more general term “molten salts”, the name “ionic liquids” is increasingly applied to salts that have a bulky asymmetric organic cation and (typically) a relatively small and symmetric inorganic anion. The term “room temperature ionic liquids” (RTILs) is often used interchangeably with “ionic liquids” and is loosely defined as those ILs that have melting points at, around, or below 100 °C. Their low volatility has made them attractive targets as substitutes for volatile organic solvents, earning RTILs their “green” reputation (at room temperature the vapour pressure of RTILs is below detection limits⁴). A broad spectrum of tunable properties arises from the customizability of the organic cation and the variety of cation-anion pairings and so ILs are often denoted as “designer solvents”. Common properties that are of central interest include negligible volatility (even at elevated temperature), wide liquidus range and ease of recycling. Ionic liquids are finding uses as solvents and reaction media in a large

number of diverse applications such as carbon dioxide sensors⁵, catalysis^{6,7}, energy storage⁸, nanostructure synthesis^{9,10}, and many others.

Anionic moieties include but are not limited to tetrafluoroborate, nitrate, perchlorate, and halides. Recently more complex perfluorated anions such as bis(trifluoromethanesulfonyl)amide or trifluoromethanesulfonate and halogen-free anions such as *n*-alkylsulphates have gained favour, as they form less hygroscopic ILs and often have reduced viscosity and increased thermal and electrochemical stability. The present work investigates halide ILs exclusively due to experimental considerations such as nuclide properties, sample availability and scope of prior work available to build upon.

Cationic moieties are equally diverse but to a large degree research has focused on 1-alkyl-3-methyl-imidazolium salts. The numbering scheme for these cations is given in Figure 1. Much of the work presented here concerns imidazolium salts, with varying alkyl substituents (methyl, ethyl and *n*-butyl) for comparison. Figure 2 depicts the cations investigated in this work and their abbreviations.

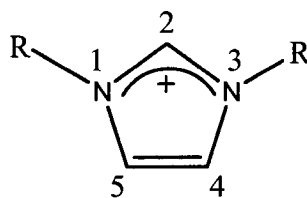


Figure 1 Numbering scheme for imidazolium cations

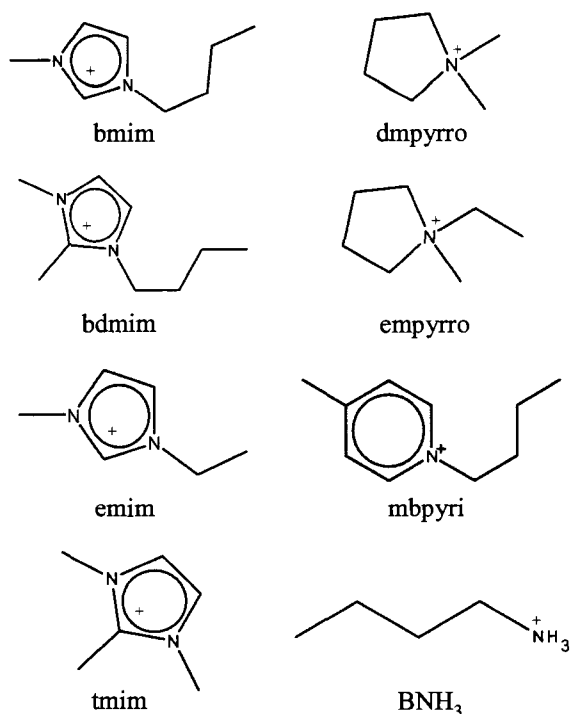


Figure 2 Cations studied in this work and their abbreviations

Due to the enormous number of potential cation-anion combinations it is impossible to investigate directly even a small fraction of the set of feasible ILs and so to develop a molecular understanding of their properties requires generalizations from representative systems. Of primary concern and controversy is the nature of the liquid state, in particular the type and extent of molecular order present. Theories, and experimental support, range from simple ion-pairs to liquid-crystal-type order depending on the characterization technique employed, the IL under study, and the interpretation of the data. It appears that only two clear trends can be distinguished that result in increased order in the liquid state: increased alkyl substituent length on the cation, and smaller anions. Furthermore even where there is agreement with regards to the presence of some kind of nanostructure, its nature is not as yet fully agreed-upon. For example, early studies led the investigators to report extended hydrogen-bonding networks, but

subsequent research has suggested that the type of bonding observed is not entirely consistent with the hydrogen-bonding model ⁴.

The present work describes an investigation into the environment of IL halide counterions in the solid and liquid states by quadrupolar nuclear magnetic resonance (NMR) spectroscopy. Subtle changes in the electronic (and magnetic) environment of a quadrupolar nucleus are readily observed by NMR and, as of this writing, this technique has not been applied to the study of solid ILs.

1.2 Nuclear Magnetic Resonance Spectroscopy

Nuclear magnetic resonance spectroscopy exploits the behaviour of atomic nuclei placed in a strong magnetic field and subjected to carefully chosen pulses of electromagnetic radiation. Nuclei possess quantized angular momentum called spin angular momentum (spin), which causes them to behave as though they are spinning about an internal axis. Nuclei with spin also exhibit a magnetic moment that is aligned either parallel or antiparallel to their spin. The spin and magnetism of a nucleus are related by a proportionality constant called the magnetogyric ratio. A semi-classical model of NMR spectroscopy is presented here to provide a brief introduction to the central concepts of the experiment.

When a sample is placed in a strong magnetic field, the spins can be oriented either parallel or anti-parallel to the field. The direction of the applied field defines the z-axis of the laboratory frame. Nuclei precess around the z-axis with a frequency determined by their magnetogyric ratio and the spectrometer's magnetic field strength,

directly analogous to the precession of a spinning gyroscope on a table under a gravitational field; this is called the Larmor frequency of the nucleus, given by

$$\omega_0 = -\gamma B_0 \quad [1]$$

where ω_0 is the Larmor frequency in rad/s, γ is the magnetogyric ratio and B_0 is the field strength.

Aligning parallel to the field is slightly more favourable energetically than an antiparallel arrangement, so a collection of spins at equilibrium has a net magnetic moment (M_z) parallel to the field. It is effectively this net magnetic moment that is manipulated by electromagnetic pulses at the Larmor frequency. The dephasing of the net magnetic moment after aligning the spins with a radio frequency pulse gives rise to the observed signal called the Free Induction Decay (FID).

To manipulate the nuclear spins the sample is placed inside a coil that is used to emit radio frequency pulses and record electromagnetic signals. The axis of the coil typically defines the x-axis of the laboratory frame. An alternating current at frequency ω_{tx} can be passed through the coil such that a magnetic field $2B_1$ is generated that oscillates along the x-axis at ω_{tx} . The magnetic field along the x-axis can be described by

$$2B_{1x}(t) = 2B_{1x} \cos(\omega_{tx}t) \quad [2]$$

This oscillating field can then be decomposed into the mathematically identical model of two fields rotating in opposite directions as illustrated in Figure 3 below.

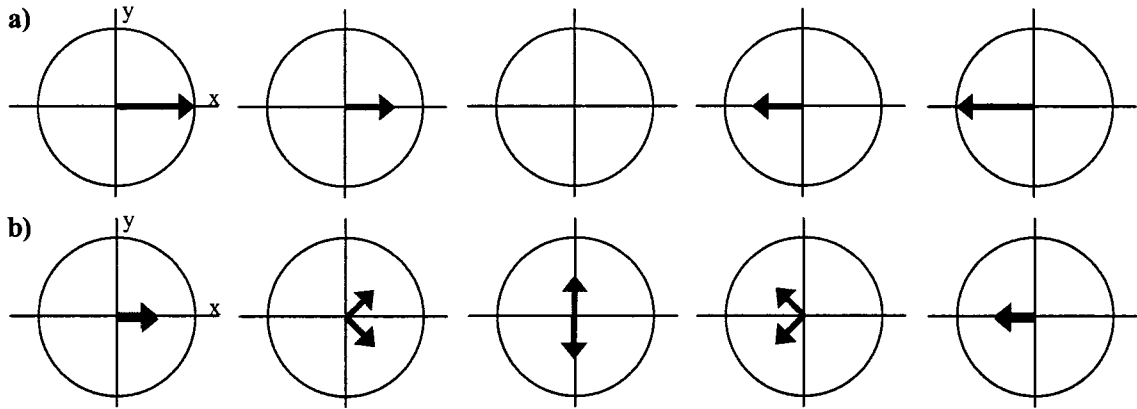


Figure 3 Decomposition of a) field oscillating along the x-axis into b) two fields rotating in opposite directions.

The decomposition can be described mathematically by

$$2B_{1x}(t) = B_{1x}[\cos(\omega_{tx})e_x + \sin(\omega_{tx})e_y] + B_{1x}[\cos(\omega_{tx})e_x - \sin(\omega_{tx})e_y] \quad [3]$$

This leads to the introduction of a convenient theoretical construct called the *rotating frame* (Figure 4). In the laboratory frame of reference there are now two fields rotating in opposite directions. If the x-y plane is assumed to rotate about the z-axis at ω_{tx} then in this rotating frame of reference (x' , y' , z') there is one stationary field B_{1x} (which defines the x' -axis of the rotating frame) and another field rotating at $2(\omega_{tx})$. The magnetization along the x' -axis is then given by

$$2B_{1x}(t) = B_{1x} + B_{1x}[\cos(2\omega_{tx})e_x - \sin(2\omega_{tx})e_y] \quad [4]$$

Then, *in the rotating frame*, the apparent precession frequency is given by $(\omega_0 - \omega_{tx})$ with the result that the static magnetic field in the rotating frame is reduced to B_{red} given by:

$$B_{red} = (\omega_0 - \omega_{tx}) / \gamma \quad [5]$$

If a transmitter frequency ω_{tx} equal to the Larmor frequency ω_0 is chosen, then the static field is reduced to zero and is no longer experienced by the nuclei. Furthermore the second term in Equation [4] can be neglected since $2 \omega_{\text{tx}} \gg \omega_0$ leaving only a static field B_{1x} along the x-axis. The rotating frame in essence turns off the static field and introduces a magnetic field generated by the transmitter as a static rather than a rotating field. All observations in an NMR experiment are made in the rotating frame and so going forward when an axis is mentioned it is a rotating frame axis.

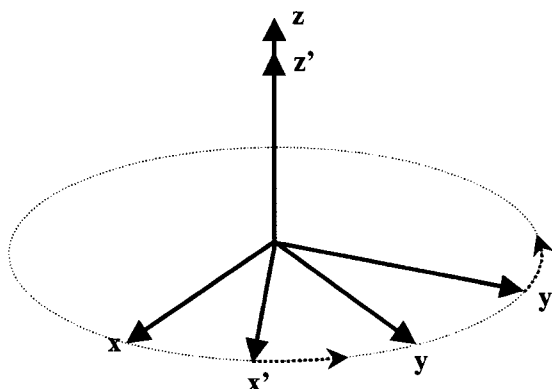


Figure 4 Stationary laboratory frame (x,y,z) and rotating frame (x',y',z')

The nuclei will then precess around this new magnetic field for as long as the pulse is maintained. Typically the duration and power of the pulse is adjusted such that the spin system is rotated (or “flipped”) 90 degrees from the z-axis. Once the pulse ends the applied field again dominates, causing the nuclei to precess in unison around the z-axis. A rotating magnetic field will induce a current in a nearby conductor and because the rotations of the nuclei are initially synchronized, their combined magnetic moments produce a signal in the coil that is strong enough to be detected. It is this signal which is then analyzed for information about the nuclei and their electronic environment. Specific

combinations of pulses and time delays can be used to further manipulate the spin system; for example to eliminate some interactions while preserving others.

After a 90° radio frequency pulse along the x-axis the resultant magnetization lies along the -y-axis (see Figure 5). This magnetization will dephase with time and as a result the signal will decay. There are two different types of signal decay: the decay as the spin system gradually drifts back to its equilibrium distribution along the z-axis, and the signal decay as the precession of the spins loses coherence. The characteristic decay time for the first type is called T_1 , the spin-lattice relaxation time. The time required for the second relaxation is called T_2 , the spin-spin (or transverse) relaxation time. The rate of decay gives insight into the properties of the nuclei and their environment. Relaxation is covered in more depth in Section 2.3.5.

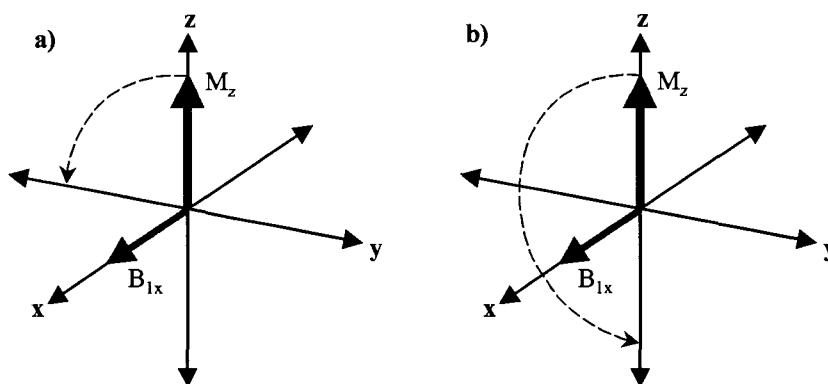


Figure 5 Precession of the spin ensemble magnetization about B_{1x} in the rotating frame by a) 90° and b) 180°

The FID is the voltage measured along a transverse axis in the rotating frame of reference. It contains time dependant signals with frequencies equal to the difference between the transmitter frequency and the frequency of the NMR lines ¹¹. The signal generated by the sample is composed of the sum of the signals generated by each nucleus as they precess around the z-axis. Nuclei in different local environments will generate

different signals. The response of a nucleus to the NMR experiment depends on the electric charge distribution of the nucleus and its magnetic moment, giving rise to chemical shift, short and long-range dipole, J-coupling and quadrupolar coupling interactions with its environment. Many of these interactions are anisotropic (orientation dependent) in the solid state and those interactions relevant to the current work are explored in detail in Chapter 2. A great deal of information can be extracted from the signal regarding the electronic and magnetic environment of the nucleus, which in turn provides information regarding molecular structure and dynamics.

Chapter 2: Solid State Quadrupolar NMR

Quadrupolar nuclei possess a spin quantum number I greater than $\frac{1}{2}$. With respect to NMR spectroscopy, such a nucleus has two very important properties: there are an increased number of possible spin states available to the nucleus, and the nucleus bears a non-spherical nuclear electric charge distribution. Spin- $\frac{1}{2}$ nuclei behave like perfect magnetic gyroscopes mounted on absolutely frictionless bearings¹², regardless of their surrounding electric field gradients. Not so for $I > \frac{1}{2}$ nuclei: because their electric charge distribution is non-spherical, their energy is dependent on their orientation with respect to the electric field gradient (EFG) at the nucleus. The EFG is created by the positions and charges of the other nuclei and electrons surrounding the nucleus, increasing in strength as the symmetry deviates from cubic¹³.

A nucleus of spin angular momentum I has azimuthal quantum numbers m associated with it, where $m = -I, -I + 1, \dots, +I$. Each value of m , along with the magnetogyric ratio of the nucleus, γ , and the strength of the applied field, B_0 , can be assigned to a spin energy level of the nucleus when placed in a magnetic (or electric) field. The spin energy levels of a nucleus of $I = 3/2$ with and without an external magnetic field are illustrated below:

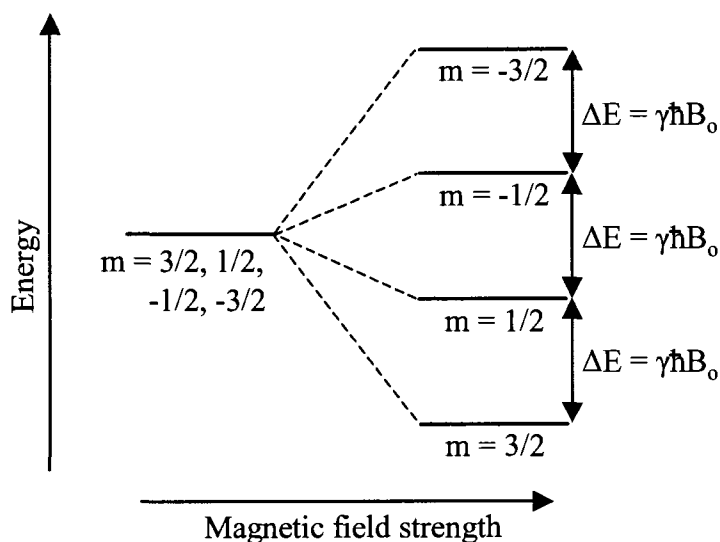


Figure 6 Spin 3/2 nuclei spin energy levels with and without an applied magnetic field. In the absence of a field, the m spin states are degenerate.

This splitting under the influence of an applied external magnetic field is called the Zeeman effect, and the resulting states and energy levels are called the Zeeman states/levels. $2I+1$ levels are seen for a nucleus with spin I , corresponding to the values of m . As illustrated in Figure 6, the transitions between levels are all of equal energy (in the absence of quadrupolar coupling). If there is quadrupolar coupling, additional changes in energy levels are observed; these can generally be sufficiently described in terms of first- and second-order corrections when the quadrupolar interaction causes splittings of less than $\sim 1/10$ of the Zeeman splitting due to the static field used in the NMR experiment ¹⁴.

The effects of these first- and second-order interactions on the energy levels of a spin-5/2 nucleus are depicted below:

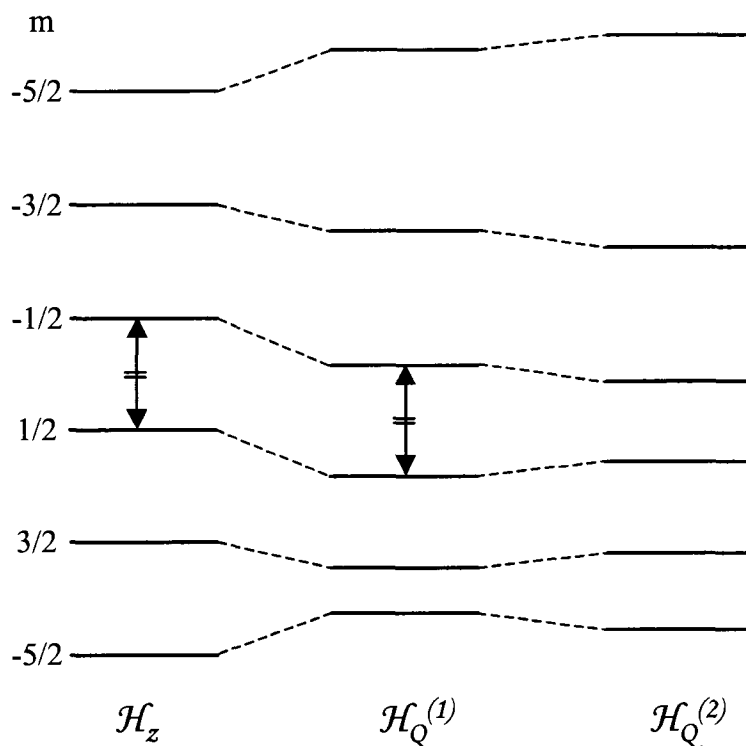


Figure 7 First- and second-order quadrupolar interaction effects on a spin-5/2 nucleus

It is important to note that the first-order energy correction has no impact on the energy of the central transition ($1/2 \rightarrow -1/2$). Thus, when the quadrupolar coupling is small a sharp peak is expected. As the quadrupolar coupling increases in strength, second-order effects are seen: the peak arising from the central transition will broaden and ultimately develop a shape in powder samples characteristic of its strength and symmetry; the satellite transitions ($3/2 \rightarrow 1/2$, $-3/2 \rightarrow -5/2$, etc.) will also change with increasing quadrupolar coupling, becoming so broad as to often be far larger than the experimental sweep width (and thus not observed). This is illustrated below:

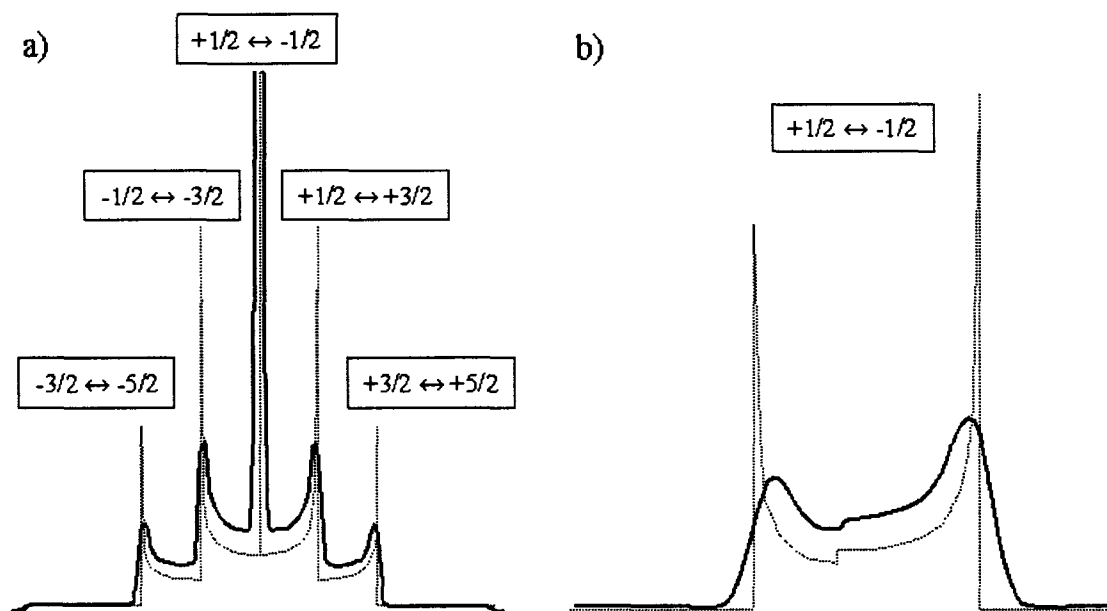


Figure 8 Quadrupolar spectra arising from a) small CQ and b) large CQ

In Figure 8a) a weak quadrupolar coupling scenario is illustrated, where only the first-order quadrupolar interactions are observed: a sharp central transition and the satellite transitions. In Figure 8b), the value of C_Q is much larger and so the shifts of the satellite transitions have spread out, with only the central transition spectrum observed. This manifests a distinct shape, reflecting the orientation dependence of the second-order quadrupolar frequency in a polycrystalline sample¹; this second scenario is observed in all samples studied in this work.

The second-order energy correction contains an isotropic term; that is, the term does not have any orientation dependence. This is an important consideration, particularly in the present work, as it means that any shift observed in the spectrum of a quadrupolar nucleus has a contribution from the quadrupolar coupling (if present) as well as from the chemical shift interactions described in Section 2.2¹³. This quadrupole induced shift is inversely proportional to the strength of the static field; if the measured shift is plotted against field strength, extrapolating to infinite field strength will yield the

true chemical shift. If in a liquid sample there are elements of order that do not allow for full isotropic averaging of a quadrupolar interaction, the residual second-order interaction may be observed as a quadrupole induced shift even though the peak may appear (at a single field strength) to be an isotropic resonance.

2.1 The Quadrupolar Interaction

The charge distribution of a nucleus can be described as the sum of a series of multipoles:

$$C(\mathbf{r}) = C^{(0)}(\mathbf{r}) + C^{(1)}(\mathbf{r}) + C^{(2)}(\mathbf{r}) + \dots \quad [6]$$

The zeroth-order multipole $C^{(0)}$ represents a spherical charge distribution, the first-order multipole describes the electric dipole moment (zero for nuclear charge distributions), the second-order term describes the electric quadrupole moment, and so on. These functions have exactly the same form as the s-, p- and d-orbitals in a hydrogen atom. The magnitudes of these functions are called the total electric charge, the electric dipole moment and the electric quadrupole moment of the nucleus, respectively.

These multipoles will interact with the electrical environment generated by surrounding nuclei and electrons. A clear relationship is seen if we represent the electric potential field by a similar superposition of terms:

$$V(\mathbf{r}) = V^{(0)}(\mathbf{r}) + V^{(1)}(\mathbf{r}) + V^{(2)}(\mathbf{r}) + \dots \quad [7]$$

Where $V^{(0)}$ is the electric potential at the centre of the nucleus, $V^{(1)}$ is the potential gradient (proportional to the difference in potential from one side of the nucleus to the other) and $V^{(2)}$ is the gradient of the gradient (the rate of change of the gradient).

The interaction energy of the nucleus with the surrounding field can be expressed as

$$E_{\text{elec}} = E_{\text{elec}}^{(0)} + E_{\text{elec}}^{(1)} + E_{\text{elec}}^{(2)} + \dots \quad [8]$$

where each term is generated by the interactions shown here:

$$E_{\text{elec}}^{(0)} = \int d\mathbf{r} C^{(0)} V^{(0)}(\mathbf{r}) \quad [9]$$

$$E_{\text{elec}}^{(1)} = \int d\mathbf{r} C^{(1)} V^{(1)}(\mathbf{r}) \quad [10]$$

$$E_{\text{elec}}^{(2)} = \int d\mathbf{r} C^{(2)} V^{(2)}(\mathbf{r}) \quad [11]$$

The first term corresponds to the point charge approximation for the atomic nucleus, representing the electrostatic forces between the nuclei and electrons and thus governing atomic and molecular structure. The second term, and in fact every subsequent odd-numbered term vanishes; within experimental error there is no nuclear electric dipole moment¹². The third term then dictates the preferred orientation of the nucleus within the field. One can imagine the surrounding electric field gradient (EFG) as a shaped potential well into which the non-spherical nucleus can settle. Since the magnetic moment of the nucleus is directly coupled to its electric moment, the EFG orients the magnetic moment as well. In contrast, due to the spherical distribution of nuclear charge in a spin-1/2 nucleus its magnetic moment will not have a preferred orientation due to the EFG, regardless of the field's asymmetry.

The magnitude of the nuclear quadrupole moment is an intrinsic property of a given nuclear species, given as eQ where e is the elementary electric charge. The strength of the interaction with the EFG depends on the magnitude of the nuclear

quadrupole moment and the strength and symmetry of the electric field gradient. The energy of a nuclear quadrupole is quantized according to its orientation in the EFG even in the absence of an applied external field. The quadrupolar interaction affects the nuclear spin energy levels *in addition to* the effect of the interaction of the nuclear magnetic dipole with any surrounding magnetic fields.

The Hamiltonian for the simplest spin system, that of an isolated spin in a static uniform magnetic field \mathbf{B}_0 , is given by the *Zeeman Hamiltonian*,

$$\hat{H} = -\hat{\boldsymbol{\mu}} \cdot \mathbf{B}_0 \quad [12]$$

where $\hat{\boldsymbol{\mu}}$ is the nuclear magnetic moment operator, which can also be written in terms of the spin operator $\hat{\mathbf{I}}$ as:

$$\hat{\boldsymbol{\mu}} = \gamma \hbar \hat{\mathbf{I}} \quad [13]$$

The quadrupole interaction Hamiltonian describing the interaction between the nuclear electric quadrupole moment of a nucleus of spin I and an electric field gradient V is (in angular frequency units):

$$\hat{H}_Q = \frac{eQ}{2I(2I-1)\hbar} \hat{\mathbf{I}} \cdot \mathbf{V} \cdot \hat{\mathbf{I}} \quad [14]$$

The EFG can be represented by a second-rank tensor and described by the nuclear quadrupolar coupling constant, C_Q , given by

$$C_Q = \frac{eV_{33}Q}{h} \quad [15]$$

and by the asymmetry parameter, η_Q , given by

$$\eta_Q = \frac{V_{11} - V_{22}}{V_{33}} \quad [16]$$

where the principal components of the diagonalized EFG tensor are arranged as

$|V_{33}| \geq |V_{22}| \geq |V_{11}|$ and e is the charge of an electron. The tensor can be described by these two independent principal components because the trace of the tensor is zero.

Below, Figure 9 presents simulations of the spectra of an ^{27}Al nucleus with an array of C_Q and η_Q values, illustrating the sensitivity of the spectra to these parameters and, more precisely, the sensitivity of the nuclei to its surroundings¹. C_Q and η_Q are determined experimentally from a collected spectrum by way of a simulation calculated to reproduce the lineshape.

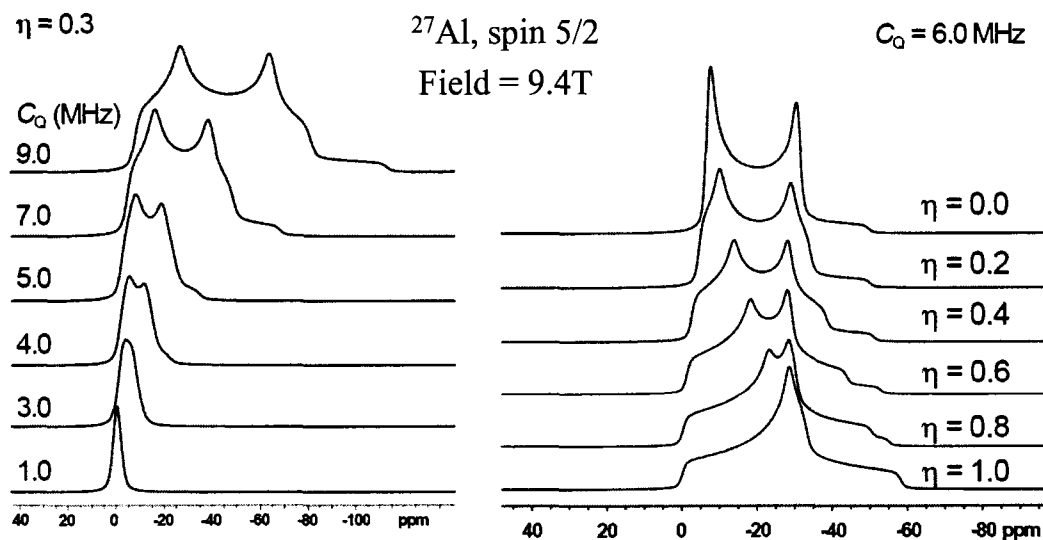


Figure 9 Sensitivity of spectra to C_Q and η_Q (credit: R.W. Schurko¹)

2.2 Shielding and Chemical Shift

The electrons surrounding a nucleus are also affected by the applied magnetic field. The nature of this interaction is such that the electrons produce a secondary field, altering the effective field felt by the nucleus and thus potentially changing its resonance frequency; it is called the shielding interaction. The changes seen in the spectrum as a consequence of this shielding is called the chemical shift. The chemical shielding (CS) Hamiltonian acting on a spin \mathbf{I} is, in frequency units:

$$\hat{H}_{CS} = \gamma \hat{\mathbf{I}} \cdot \boldsymbol{\sigma} \cdot \mathbf{B}_0 \quad [17]$$

The second-rank tensor $\boldsymbol{\sigma}$, called the chemical shielding tensor, is used to describe the extent of the shielding and its dependence on molecular orientation. The axis frame of this tensor, called the principal axis frame, is chosen such that the tensor is diagonal. The principal values of the shielding tensor are seldom given; often a set of quantities based on these values is given instead to provide a more intuitive representation of the strength of the interaction and its orientation dependence. In this work these are expressed as the isotropic value δ_{iso} , the span Ω and the skew κ , as follows:

$$\delta_{iso} = \sigma_{ref} - \frac{\sigma_{11} + \sigma_{22} + \sigma_{33}}{3} \quad [18]$$

$$\Omega = \sigma_{33} - \sigma_{11} \quad [19]$$

$$\kappa = \frac{3(\sigma_{22} - \sigma_{iso})}{\Omega} \quad [20]$$

Where σ_{11} , σ_{22} and σ_{33} are the principal values of the shielding tensor. In a simple spectrum, the components of the tensor can be determined experimentally from chemical shift powder patterns as illustrated in

Figure 10. In more complicated spectra where multiple sites and/or interactions are present, the components can be determined experimentally from a collected spectrum by way of a simulation calculated to reproduce the lineshape, as with the quadrupolar interaction.

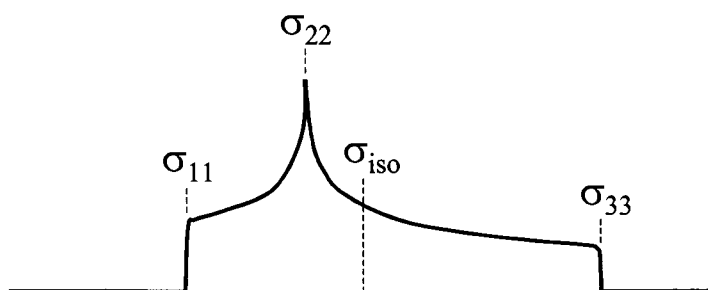


Figure 10 Determining CSA parameters from a spectrum

The observed powder patterns arise from the multitude of random orientations of the CS tensors in a powdered sample. The orientation dependence of each CS tensor arises from the interaction of the static magnetic field with the local three-dimensional electronic structure. In the liquid state, isotropic tumbling ensures that the nuclei in a molecule see only an average of all possible orientations and the orientational effects are eliminated. In the solid state, nuclei in a given molecule will see a field modified according to that particular molecule's symmetry and orientation with respect to the field. The examples in Figure 11 illustrate the relationship between the three-dimensional distribution of electrons and the impact on lineshape in a polycrystalline sample. The

various orientations of the molecules in a polycrystalline sample will contribute to generate these types of patterns.

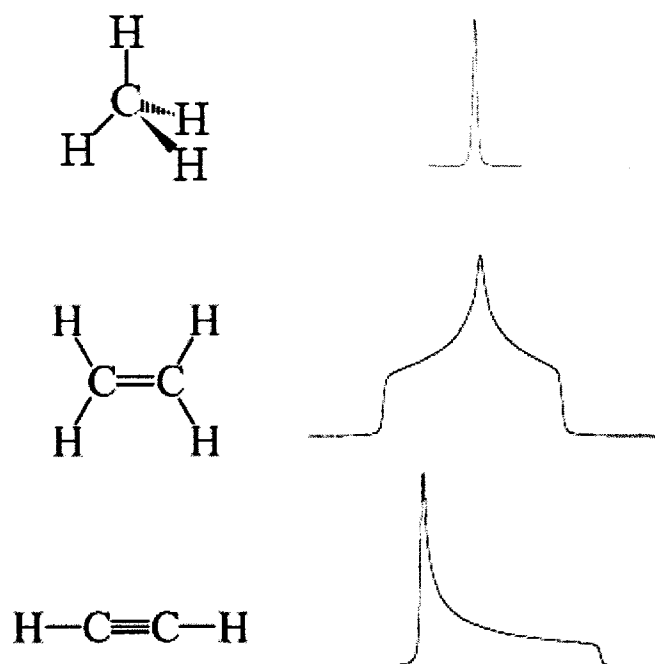


Figure 11 Examples of symmetry of the chemical shift tensor and the resulting CSA powder patterns; a) spherical, b) non-axial (shielding is different in all three directions) and c) axial

The combination of simultaneous quadrupolar and CS interactions can lead to further complexity. The principal axes of the tensors that describe these two interactions are often not coincident and so their relative orientation must be considered. This is described by the set of rotations required to obtain the proper relative orientation of the axes of the tensors, in terms of the *Euler angles* α , β and γ . In this work the convention of Mehring is followed¹⁵: starting with coincident tensor axes and effecting counterclockwise rotations of the CS tensor (here described by its principal axes σ_{xx} , σ_{yy} and σ_{zz}), α describes the initial rotation about the original σ_{zz} axis, β is a rotation about the

direction of σ_{yy} resulting from the first rotation and γ is the rotation about the direction of σ_{zz} resulting from the first and second rotations (also known as the ZYZ convention).

The process is illustrated in Figure 12 below.

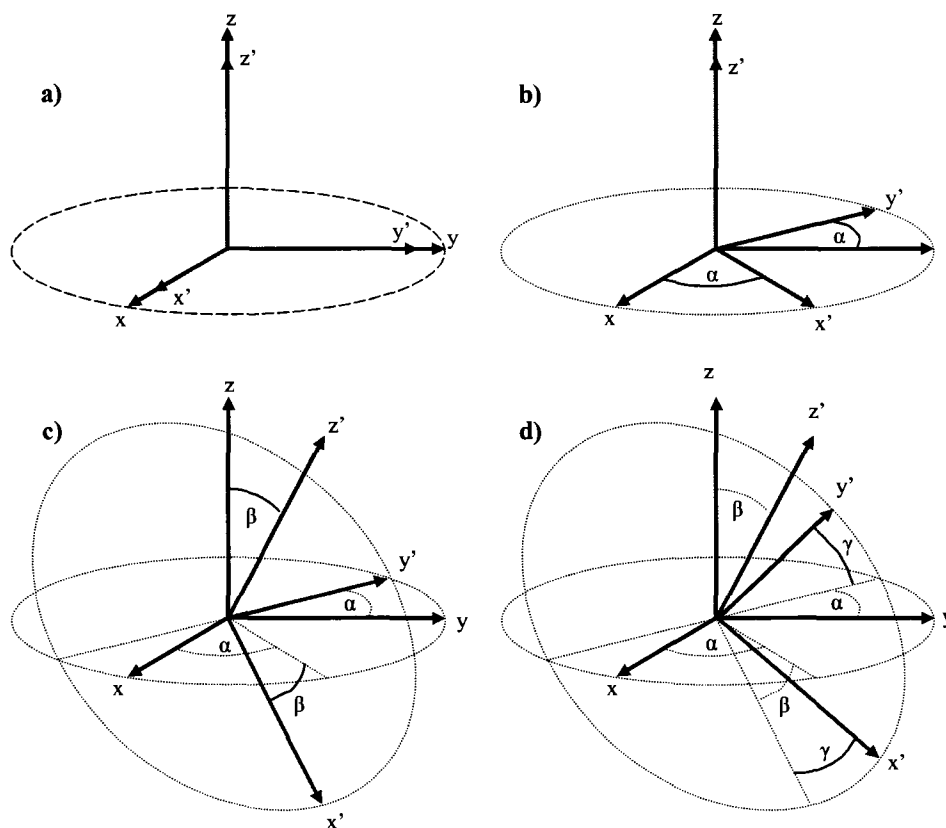


Figure 12 Describing the relative orientation of two axis systems, beginning with a) aligned axes then b) rotating about the z -axis by α , c) rotating about y' by β and finally d) rotating about z' by γ

2.3 Quadrupolar NMR techniques

In this section, NMR techniques useful in the study of quadrupolar nuclei are reviewed. In the liquid state, anisotropic nuclear spin interactions vanish. The isotropic

motion of the liquid serves to average out interactions that are anisotropic in the solid-state. In the past, these interactions were obstacles to the recording and interpretation of solid-state spectra however advances in technology and techniques have improved such that these interactions can now be exploited to determine features of molecular structure and molecular dynamics by methods not available to liquid state studies.

2.3.1 Magic Angle Spinning

Magic Angle Spinning (MAS) has a variety of uses in solid-state NMR spectroscopy. In this work only its ability to remove chemical shift anisotropy effects will be considered. Removing the line broadening introduced by CSA is useful for revealing multiple inequivalent nuclear sites whose powder patterns overlap. It can also be used to facilitate the extraction of quadrupolar parameters from spectra.

The effects of CSA are not generally seen in solution NMR. This is due to the rapid isotropic tumbling of the molecules. The orientation dependence of the CSA is effectively removed because on the timescale of the NMR experiment, the electrons in the sample see the same field from all directions while the nucleus remains aligned by the applied field. In a powdered solid sample all molecular orientations are present but they are not tumbling and so each orientation gives rise to a specific frequency, producing a powder pattern (see Figure 13). MAS can be employed to simulate solution conditions.

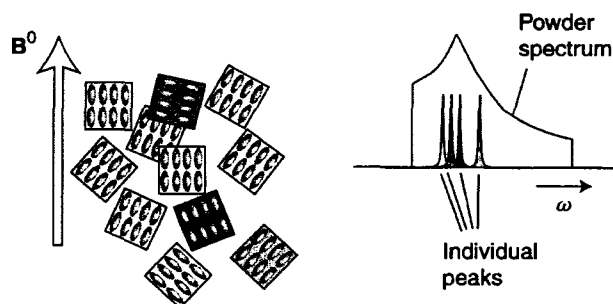


Figure 13 Origin of the CSA powder pattern

If we spin a sample using the configuration shown in Figure 14, the average orientation dependence of the nuclear spin interaction, $(3\cos^2\theta-1)$ can be shown to be

$$\langle 3\cos^2\theta - 1 \rangle = \frac{1}{2} (3\cos^2\theta_R - 1) (3\cos^2\beta - 1) \quad [21]$$

where the angle β is between the principal z-axis of the shielding tensor and the spinning axis, θ_R is the angle between the applied field and the spinning axis and θ is the angle between the principal z-axis of the interaction tensor and the applied field \mathbf{B}_0 . If θ_R is set to 54.74° , then $(3\cos^2\theta_R - 1) = 0$ and the average goes to zero. The sample must be spun fast enough to average theta rapidly compared to the anisotropy for the effects of the CSA to be removed.¹³

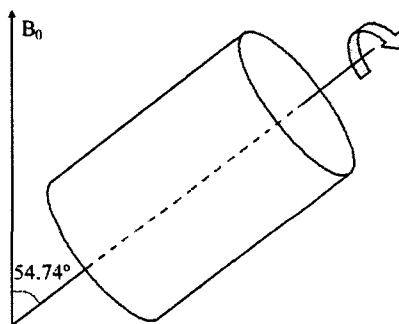


Figure 14 MAS experimental set-up, where \mathbf{B}_0 is the applied magnetic field and the sample rotor is rotated about an axis oriented at an angle of 54.74° to the field

Spinning at a rate that is too slow will either have no effect, or produce so-called spinning sidebands. These manifest as lines flanking the isotropic chemical shift at intervals equal to the MAS spinning rate. While spinning sidebands have experimental uses, these were not employed in the current work. A good practical rule of thumb is that the spinning rate should at least be equal to the width of the powder pattern, ideally on the order of three times the frequency.

MAS will alter, but not eliminate the effects of a quadrupolar interaction on a spectrum: the first-order quadrupolar interaction effects discussed at the beginning of this section will be averaged out with sufficiently fast spinning, but the second-order interaction does not depend simply on $3\cos^2\theta - 1$, and so its effects are not averaged out by MAS. These effects can be averaged out by *double rotation* (DOR) where the sample is spun simultaneously at two angles; the magic angle of 54.74° which eliminates the first-order effects and either 30.6° or 70.1° which averages out the second-order effects. DOR is not employed in the present work, but DOR probes are available.

Under MAS the width of a lineshape resulting from a quadrupolar coupling is reduced and its shape changes somewhat due to the elimination of first-order effects. The parameters of its tensor can still be determined from the resulting lineshape.

Correspondingly, if there is a molecular arrangement in a sample such that there exists a quadrupolar coupling interaction that is tumbling isotropically (for example structural elements in an otherwise liquid environment) then the second-order quadrupolar interaction effects can still manifest in the observed spectrum: the chemical shift is dependent upon field and so for such a system, spectra taken at different field strengths will exhibit different apparent chemical shifts¹⁶. We note that this shift disappears when

the averaging motion is sufficiently fast, i.e. when the correlation time (discussed in Section 2.3.5) is close to the inverse of the Larmor frequency ($\tau_c \sim 1/\omega_0$). This property is exploited in the current work; results are presented in Section 4.2.2.

2.3.2 Hahn Echo and Solid Echo Pulse Programs

The FIDs of the signals acquired in this work are often quite short (10 μ s - 5 ms), meaning that the signal decays quickly. Due to experimental limitations there must be a delay after a pulse before acquisition can begin, which may mean that the beginning of the FID is not acquired. For this work the beginning of the FID is of particular importance as it contains information pertaining to broad signals. A Fourier transform is employed to convert the FID signal to an NMR spectrum; it is a mathematical conversion between time domain functions (FID's) and frequency domain functions (NMR spectra). Signals in the FID that are sustained for a long time correspond to sharp peaks in the frequency domain, and brief signals correspond to broad peaks. In this work all peaks are relatively broad.

To ensure that the full FID is acquired, Hahn Echo and Solid Echo pulses were employed. The Hahn Echo pulse sequence employs a $(\pi/2)_x$ pulse, a delay τ_1 , then a π_x pulse followed by a second delay τ_2 and then FID acquisition. τ_1 allows the magnetization from the first pulse to evolve as it will. The π_x pulse (which can also be a π_y pulse) inverts the magnetization, which will then proceed to refocus. If the acquisition is begun immediately after the second pulse ($\tau_2 \approx 0$), the resulting signal resembles a FID in reverse as the magnetization refocuses, followed immediately by a typical FID; this is called a “whole echo” acquisition. If the acquisition begins just as the magnetization has

completed refocusing this is called a “half-echo” acquisition. The Solid Echo pulse sequence is very similar to the Hahn Echo; the only difference is in the second pulse which is a $(\pi/2)_x$ instead of π_x . Acquisition can then proceed as described above. An empirical approach was employed to choose the best pulse program for a given sample.

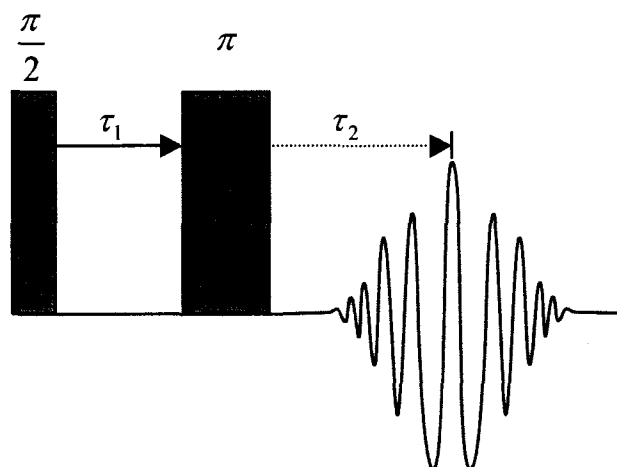


Figure 15 Hahn Echo pulse sequence

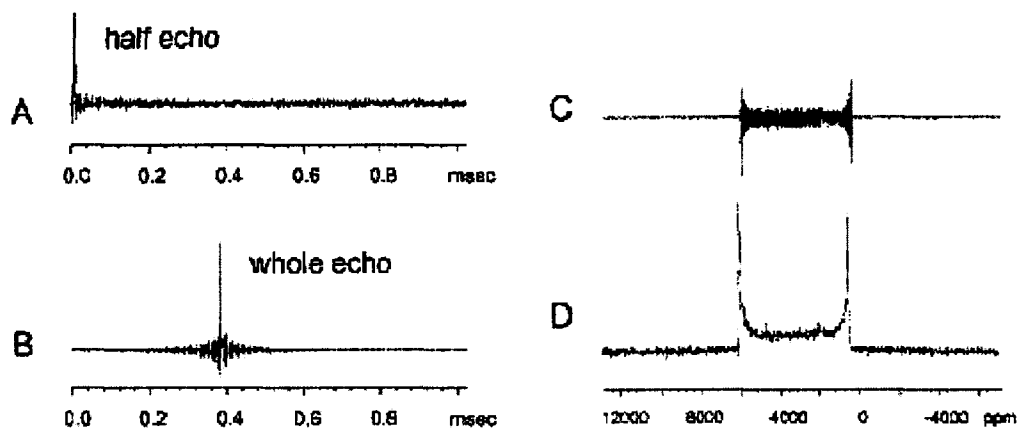


Figure 16: (A) Half-echo 127I FID. (B) Whole-echo 127I FID. (C) The direct FT of the whole-echo FID shown in (B). (D) FT followed by first-order phase correction of the whole-echo FID shown in (B). The sample is NaIO_4^{2-}

2.3.3 Proton Decoupling

Heteronuclear dipolar coupling can affect the quality of the signal collected, even under magic angle spinning. Dipolar coupling is the through-space interaction of the magnetic moments of nuclear spins. Powder pattern features useful for the determination of EFG and CSA parameters can be broadened significantly, as in the case of the chlorine spectra in this work. Fortunately this broadening can be eliminated relatively easily with high-power, long-duration radio-frequency pulses.

The ^{35}Cl - ^1H dipolar coupling can be eliminated by applying continuous irradiation of sufficient power (100-1000 W) at the proton resonance frequency while the ^{35}Cl FID is acquired. The effect of the continuous pulse, simply put, is to cause the ^1H spins to undergo repeated transitions from $+1/2$ to $-1/2$. The amplitude of the pulse determines the rate of these transitions. At a sufficiently high rate the ^{35}Cl spectrum will only be influenced by the time-averaged dipolar coupling, which will be equal to zero. In other words, the magnetic dipoles of the ^1H spins are alternating so rapidly with respect to the NMR experiment that their magnetic influence on the ^{35}Cl nuclei is eliminated.

2.3.5 T_1 and T_2 Relaxation

When a sample is placed in the magnetic field of a spectrometer, the randomly oriented spins of the nuclei gradually align with the field and the longitudinal (z-axis) magnetization of the system builds up, with the form

$$M_z(t) = M_{z,eq}(1 - e^{-t/T_1}) \quad [22]$$

The exponential time constant in this equation, T_1 , is known as either the *spin-lattice relaxation time constant* or the *longitudinal relaxation time constant*. From the above equation it can be seen that T_1 is the time it takes for a sample to recover 63% of its maximum magnetization in the z-direction. This depends on the nucleus and nature of the sample in question, as well as the temperature, viscosity, and other factors. Typical values are found on the scale of microseconds or seconds, but can last as long as days and years¹².

The magnitude of z-magnetization is exceedingly small and impractical to study directly experimentally. The rotating magnetic field resulting from transverse magnetization is much more readily detectable. Like longitudinal magnetization, transverse magnetization also has a sample and condition-dependent time constant, called T_2 . T_2 is the time it takes for the radio-frequency-induced transverse magnetization to drop to 37% of its original magnitude, as seen in the equation

$$M_{xy}(t) = M_{xy}(0)e^{-t/T_2} \quad [23]$$

where $M_{xy}(0)$ is the transverse magnetization immediately after a 90° pulse. Upon being flipped into the x-y plane, the nuclei initially precess in a synchronized fashion due to the applied magnetic field. In the vector model of spin dynamics, one can describe this process as an initially coherent vector in the rotating frame fanning out into many vectors precessing in opposite directions as various interactions cause the spin system to become decoherent. This process clearly manifests in the rate at which an FID signal's amplitude decreases into the noise over time.

Differences in the local field felt by the individual spins are responsible for this dephasing of coherence, caused by the magnetic fields of nearby nuclear spins which may have completely random orientations. T_2 is variously referred to as the *transverse relaxation time constant*, *coherence dephasing time constant*, *coherence decay time constant* and *spin-spin relaxation time constant*. T_2 values are of the same order magnitude as T_1 in liquids, but can be much shorter than T_1 in solids. For a given sample T_2 can never exceed T_1 ; a sample cannot have recovered its full z-magnetization and still retain some transverse magnetization. T_2^* is similar to T_2 in that it describes the same relaxation process, but it incorporates the inhomogeneities of the field experienced by the spins due to irregularities in the applied static field. T_2^* is always smaller than T_2 , and is given by

$$\frac{1}{T_2^*} = \frac{1}{T_2} + \frac{1}{T_{\text{inhom}}} = \frac{1}{T_2} + \gamma\Delta B_0, \quad [24]$$

where γ represents the gyromagnetic ratio and ΔB_0 is the strength of the locally varying field.

Measurement of T_1

T_1 can be measured using sequences of pulses and delays that manipulate the spin system, providing information about molecular motion and dynamics. A commonly used technique is *inversion-recovery*. The figure below illustrates the pulse sequence:

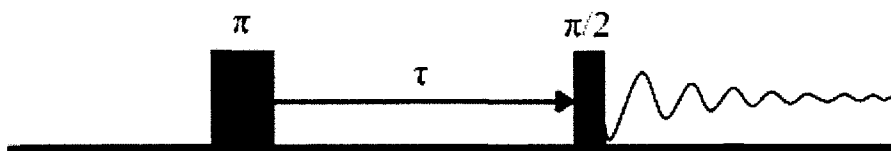


Figure 17 Inversion-recovery pulse sequence and FID. Acquisition begins after $\pi/2$ pulse.

A π pulse is followed by a time delay, which is followed by a $\pi/2$ pulse and FID acquisition. A number of spectra are collected, with increasing delay time τ . This generates a two-dimensional data set of spectra, each with a unique time delay. The time between the last pulse of one sequence and the first pulse of the next sequence must be several times longer than T_1 in order to recover full z-magnetization, so an initial best guess at T_1 must be used to set up the sequence.

In terms of vector dynamics, an initial π_x pulse (for example) places the vector along the $-y$ axis. If left alone, the vector will shrink along the $-y$ -axis and then grow along the y -axis as the spins re-align themselves with the applied static field. The progress of this reversal is monitored by applying the $\pi/2$ pulse, which flips the vector into the transverse plane, followed by FID acquisition. As the delay is increased, the intensity of the resulting peak will increase from a negative minimum to a positive maximum. The process is shown below in Figure 18. The curve is then fit to Equation [20] to extract T_1 .

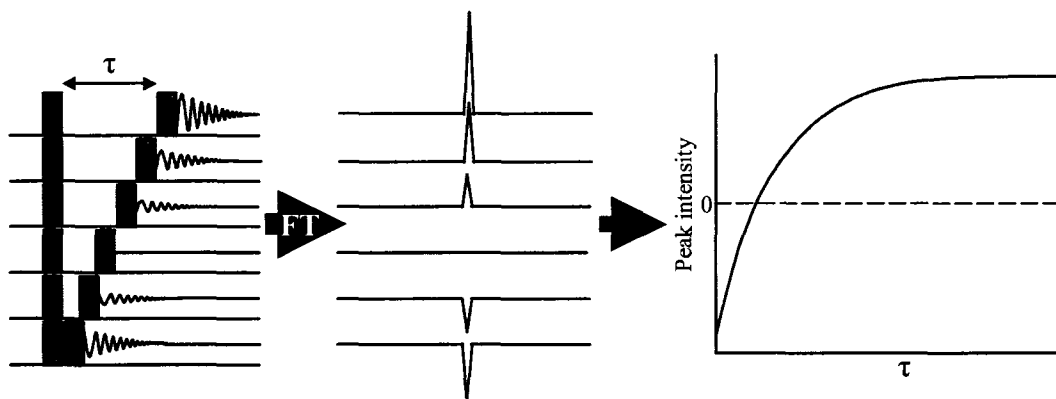


Figure 18 The inversion-recovery experiment. Peak intensity is plotted against time delay τ .

For a sample containing different spin ensembles, such as different chemical compounds, different isotopomers of the same compound, or if different regions of the

sample experience significantly different magnetic fields (as in a gradient) then multiple peaks may be seen, each with their own T_1 response.

Measurement of T_2

Ideally T_2 could simply be measured from the width of the peak of interest, since for an homogenous applied field the width-at-half-height in Hz is given by $1/(\pi T_2)$. Broadening due to macroscopic variations in the magnetic field, mainly due to instrumental limitations, alters this relationship; the peak is broadened beyond the contribution from the decay of transverse magnetization. In an experimental setting the relaxation constant derived from this method is called T_2^* .

Fortunately a Hahn echo (or spin echo) pulse sequence can be used to accurately measure T_2 despite field irregularities, shown here:

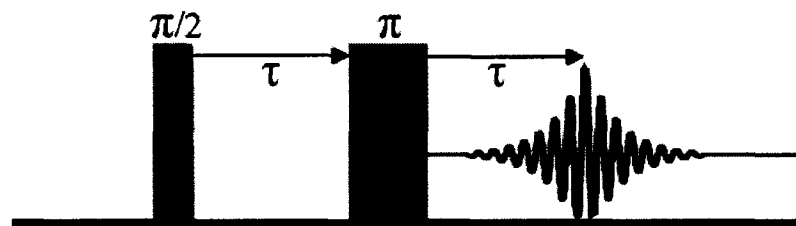


Figure 19 Hahn echo pulse sequence and resulting FID. Signal acquisition begins after π pulse.

The delay τ between the two pulses gives the magnetization time to dephase, and matches the time it takes for the peak intensity of the echo to manifest after the π -pulse. The echo is a refocusing of the spin vectors that lost coherence after the $\pi/2$ -pulse. An FT of the FID can be taken from the peak of the echo, or one can FT the entire echo and use phase correction to adjust the resulting peak. An arrayed experiment is performed, varying the delay between pulses. The resulting data array can be analyzed to obtain the

value of T_2 by plotting a graph of peak intensity versus delay, similar to the process illustrated in Figure 18.

Relaxation Mechanisms

There is a large distribution of frequencies of motions of the molecules in a sample of a typical liquid; some molecules are moving slowly while others are moving quite rapidly. A useful model when considering relaxation mechanisms is to consider the time a “typical” molecule remains in any given position, called the *correlation time*. Each collision will change a molecule's state of motion. If, for example, a molecule performs a motional jump every 10^{-12} s, one can expect that its motion will have frequency components from 0 to 10^{12} Hz (similar to the frequency components of a very short radio frequency pulse).

Low frequency (slow) processes only affect the spin-spin relaxation time T_2 and not the spin-lattice relaxation time T_1 , whereas high frequency processes (at the resonance frequency and higher) affect both T_1 and T_2 ¹⁷. Low frequency interactions are the reason why T_2 is often shorter than T_1 , as when chemical exchange, diffusion, or other similar, relatively low frequency processes are present.

In general, in addition to molecular motions, any mechanism which gives rise to fluctuating magnetic fields at a nucleus can contribute to relaxation, for example: the magnetic dipole-dipole interaction, electric quadrupole interaction, chemical shift anisotropy interaction, spin-rotation interaction, and field inhomogeneity. Figure 20 shows the general relationship between T_1 , T_2 , and temperature (and therefore molecular motion), and the nature of the molecular organization in a sample.

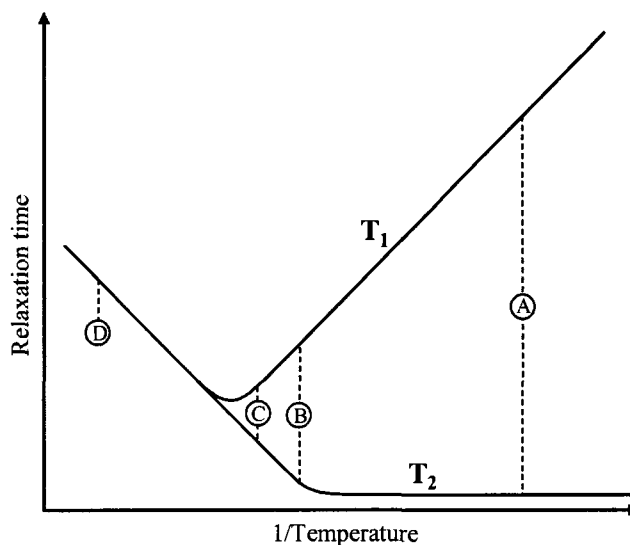


Figure 20 Schematic illustration of the dependence of relaxation times on temperature

The position on Figure 20 labelled **A** corresponds to the “rigid lattice” of a solid. Very slow molecular motions allow for a large T_1 while the anisotropic interactions, many of which increase in intensity with decreasing temperature, result in a short T_2 . The situation labelled **B** corresponds to a scenario where there may exist significant structural elements but molecular motion is much greater than that of a rigid solid. The ratio of T_1 to T_2 in this region will be much higher for cross-linked polymers near room temperature than, for example, an ionic solid undergoing a melt. Similarly, Case **C** corresponds to a viscous liquid sample and **D** to a nonviscous liquid where $T_1 \approx T_2$; this last region is referred to as the “fast motion limit”. Experimentally, the T_1/T_2 ratio of a sample in the regime near **B** and **C** can provide clues as to the existence and nature of any structural elements in the liquid phase of a sample. Results of such experiments in this work are reported in Section 4.2.2.

2.4 Simulations and Computational Methods

2.4.1 DMfit

The DMfit program, written by D. Massiot et al enables fitting of solid- and liquid-state NMR spectra¹⁸. The QUASAR module, written by Jean Paul Amoureux for computing spectra under static or MAS conditions with multiple interactions was used for simulation of the CSA parameters of solid static samples¹⁹.

2.4.2 Bruker Topspin

The Bruker Topspin suite is a software package for acquisition, processing and analyzing NMR data. In this work it was used to acquire spectra on the 21.1 T instrument, process and produce spectra for publication, and simulate MAS spectra. Simulations were performed using the “Solid state lineshape analysis” function, which computes various line shape models and fits them to spectra. The version used (v.1.3) was not capable of simulating the effects of CSA on spectra and so DMFit was used for this task.

2.4.3 Gaussian 98

Computational methods were used to calculate the quadrupolar coupling constant, asymmetry parameter, isotropic chemical shift, span and skew. The calculated values were then compared to the values extracted by spectrum analysis. All calculations were performed using the Gaussian 98 program²⁰.

From the manual: Gaussian 98 is a connected system of programs for performing a variety of semi-empirical and *ab initio* molecular orbital calculations. Computations can be carried out on systems in the gas phase or in solution, and in their ground state or in an excited state. Thus, Gaussian 98 can serve as a powerful tool for exploring areas of chemical interest like substituent effects, reaction mechanisms, potential energy surfaces, and excitation energies.

Chapter 3: RTIL Solid- and Liquid-state Structure

What follows is a survey of techniques and results in the literature pertaining to the liquid and solid structure of ionic liquids, with a focus (where possible) on prior studies of the ionic liquids investigated in this work.

The molecular interactions between ions are governed by their geometry and their charge strength and distribution. In simple salts (small symmetric ions) long-range Coulombic forces between the net charges of the ions dominate the interactions. The bulky and asymmetric charge distribution in the molecular ions typical of ILs reduces the influence of these long-range forces and highly directional short-range interactions become dominant; for example between the π -systems of aromatic rings or hydrogen bonds⁴. The role of hydrogen bonding in these materials is currently the subject of much debate.

There is no common agreement among studies as to the nature of long-range liquid-state RTIL order; depending on the system examined some studies show support for ion-pair formation, others indicate varying degrees of aggregation and still others suggest a crystal-like organization (albeit a 'fragile' and likely transient one).

3.1 Solution NMR

In a comprehensive 2007 review of magnetic resonance spectroscopy in ionic liquids by Giernoth and Bankmann²¹, only one paper is cited that employs ^{35}Cl and ^{127}I NMR²² in work done by Welton et. al.; the vast majority of studies cited focus on ^{13}C and ^1H nuclei but no other studies employed halogen NMR. Evidence presented by Welton's group, gathered from ^{35}Cl and ^{127}I NMR and conductivity measurements of emim-halide RTILs confirmed the formation of strong hydrogen bonds between halide anions and all three imidazolium ring protons. The authors conclude that RTILs "must now be considered not as statistical aggregates of anions and cations, but as a three-dimensional network of anions and cations, linked by a network of fragile hydrogen bonds". Carper et al. share this view, based on their investigation of the reorientational dynamics of 1-butyl-3-methylimidazolium hexafluorophosphate by measurement of ^{13}C spin-lattice relaxation rates and NOE factors. The authors state that ionic liquids may have "a kind of layer structure, in which the anions are located mainly above and below the aromatic ring"²³.

In the present work quadrupolar nuclei are employed as a promising and previously largely unexplored probe of the intermolecular interactions in both the solid and liquid states of RTILs.

3.2 Computer Simulation

Simulations of the structure, dynamics and bulk properties of ILs allow investigators to work around experimental limitations. Often the reliability of such simulations depend upon the quality of the molecular force field used; it remains difficult to develop predictive and transferable force fields due in part to the lack of experimental data available (such as enthalpies of vaporization) ⁴.

Ab initio quantum chemistry calculations are computational methods that can be useful when little experimental data is available. The term *ab initio* indicates that the calculation is from first principles and that no (or, in practice, limited) empirical data are used. Several *ab initio* studies have been performed investigating the nature of intermolecular interactions in ILs. In the majority of these, the authors assume or conclude that intermolecular hydrogen bonding is of primary importance. More specifically with respect to imidazolium-based ILs, there is general agreement that the strongest such interaction is between the C2 hydrogen of the imidazolium ring and the counteranion (see Figure 1 on p.6 for numbering scheme) ²⁴⁻²⁸. The timescale of *ab initio* calculations are typically on the order of picoseconds ²⁹.

In contrast, work by Katsyuba et al. analyzing IR and Raman spectra within the framework of scaled quantum mechanics indicated that, although features of the spectra are explained by hydrogen-bonding, the Coulomb interactions between the ions are of greater importance²⁶. Furthermore, Tsuzuki's group studied the intermolecular interaction energies of imidazolium-based ionic liquids by MP2/6-311G** level *ab initio* calculations and concluded that "the nature of the C₂-H...X interaction is considerably different from that of conventional hydrogen bonds". In particular, they concluded that

the size of the interaction energy between the anion and the cation is mainly determined by proximity of the anion to the imidazolium ring; the orientation of the anion relative to the C₂-H bond did not greatly affect the size of the calculated interaction energy. They point out that this does not fit the profile of hydrogen-bonding, which is highly directional³⁰.

Ludwig, Heintz, Wertz and Köddermann, using a combination of FTIR measurements and DFT calculations, performed a relevant investigation with regards to long-range structure in liquid RTILs. They studied ion-pair formation in 1-ethyl-3-methylimidazolium bis(triflyl)imide as a function of temperature and concentration. Assigning IR spectral peaks by way of DFT calculations for a number of neat ion pairs as well as larger structures, the authors show that “the three-dimensional structure found in the solid state is maintained in the liquid phase” and “the neat IL is mainly organized as an H-bonded polymeric supramolecule”. They state further that this supramolecular structure coexists at 273K with significant numbers of simple ion pairs, comprising approximately 20% of all ions²⁸.

As of this writing, the present work includes the first ab initio calculations of the NMR properties of chlorine nuclei in ionic liquids.

3.3 Neutron Diffraction

Neutron diffraction is a crystallographic method used to determine the atomic structure of a material. The technique is similar to X-ray diffraction but the use of neutrons provides complementary information. Being uncharged, neutrons scatter much

more strongly from the atomic nuclei rather than from the electrons; this is useful for observing the positions of light atoms with few electrons, especially hydrogen, which can be difficult to detect by X-ray diffraction. However obtaining intense, monochromatic beams of neutrons in sufficient quantity, and the expense and availability of necessary isotopes, can be problematic ³¹.

Neutron diffraction work by Hardacre, Holbrey, McMath, Bowron and Soper leads the authors to conclude that there is significant charge ordering in the liquid state of 1,3-dimethylimidazolium chloride ([dmim][Cl]), and that “the molecular packing and interactions in the first two or three coordination shells are similar in both the crystal and the liquid” (with an increase in absolute distances upon melting) ³². In a second study by Hardacre, McMath, Nieuwenhuyzen, Bowron and Soper the authors reached a similar conclusion for [dmim]hexafluorophosphate ([PF₆]⁻); namely, that the crystal and liquid structures “correlate well” ³³. It is interesting to note, regarding the discussion of hydrogen bonding in RTILs in Section 3.2, that the authors find that the overall structures of the chloride and [PF₆]⁻ salts are very similar despite the difference in hydrogen bonding ability. A third paper in this series, by Deetlefs, Hardacre, Nieuwenhuyzen, Padua, Sheppard and Soper, presents neutron diffraction work on [dmim]bis{(trifluoromethyl)sulfonyl}amide ([NTf₂]⁻). The authors found significantly smaller charge ordering compared to the chloride and hexafluorophosphate salts, which they attribute to the diffuse charge density and size of the [NTf₂]⁻ anion. The authors further state that there is little correlation seen between the crystal and liquid structures, with the [NTf₂]⁻ anion adopting a trans configuration in the liquid and a cis configuration in the solid phase. Taken together, these studies demonstrate the tunability of ionic

liquids and reinforce the need for caution regarding broad statements about the properties and characteristics of systems with dissimilar ions.

3.4 X-ray diffraction

X-ray diffraction is a technique for determining the arrangement of atoms within a crystal from the manner in which a beam of X-rays is scattered from the electrons within the crystal. The method produces a three-dimensional map of the density of electrons within the crystal, from which the mean atomic positions, their chemical bonds, their disorder and other information can be derived. It has the advantages of high flux and the fact that scattering is proportional to atomic number. Disadvantages include the greater difficulty in locating hydrogen atoms and the inability, in general, to obtain data on long-range order from a liquid.

Crystal structures obtained by x-ray diffraction were available in the literature for five of the twelve RTILs studied in this work: emim[Cl, Br], bmim[Cl, Br] and bdmim[Cl], as described below.

In their study of solid emim[Cl], Adams et al. determine that the orthorhombic space group is $P2_12_12_1$, with $a=10.09$, $b=11.18$, $c=28.73$ Å, and that the asymmetric unit contains four emim[Cl] ion pairs³⁴. The crystal structure is characterized by interspersed layers of cations and anions, with the directions of the cation stacks in adjacent layers rotated by 90°. They conclude that each cation is hydrogen bonded at the three ring carbon atoms to the three nearest chloride anions. Further investigations in the same work show similarities between the liquid and solid structures by FTIR, discussed in Section 3.5.

Welton et al. show that in solid emim[X] (X=Br or I) the local structure around the cation is superficially similar to that observed for emim[Cl], but that the overall morphology of the crystals is significantly different²². The Br⁻ and I⁻ salts are less complicated, with only one unique cation and one unique anion, whereas the Cl⁻ salt has four of each, as mentioned above. The authors suggest that the size differences of the halide ions are responsible for the structural differences. For emim[X] (X=Br or I) they find that the monoclinic space group is $P2_1/c$, with $(a, b, c)_{Br}=(0.88, 0.80, 1.27 \text{ \AA})$ and $(a, b, c)_I=(0.88, 0.81, 1.34 \text{ \AA})$ where $\beta = 109.91^\circ$ and 107.33° for the Br and I salts respectively.

Holbrey, Reichert, Nieuwenhuyzen, Johnston Seddon and Rogers determined the crystal structures of solid bmim[Cl] and bmim[Br] by single crystal X-ray diffraction³⁵. They report two polymorphs for the chloride: an orthorhombic form (I), isomorphous with the bromide structure, and a monoclinic form (II). The distinguishing difference between the two chloride polymorphs is an all-*gauche* butyl chain in (I) and an *anti* conformation of the butyl chain in (II). Crystal data for the chlorides: $(a, b, c)_I=(10.11, 11.41, 8.33 \text{ \AA})$, space group $Pna2_1$ and $(a, b, c)_{II}=(9.94, 11.48, 9.66 \text{ \AA})$, space group $P2_1/c$, $\beta=118.74^\circ$. For the bromide salt, $(a, b, c)=(10.06, 11.86, 8.43 \text{ \AA})$ with space group $Pna2_1$.

Kölle and Dronskowski used single crystal X-ray diffraction to determine the structure of bdmim[Cl]: a monoclinic cell containing four formula units and space group $P2_1/n$, with $(a, b, c)=(838.0, 1171.0, 1076.0 \text{ \AA})$ and $\beta=90.74^\circ$ ³⁶.

3.5 Raman and FTIR Spectroscopy

Work by Hamaguchi, Ozawa and Hayashi indicates that there exist two distinct structures of the bmim^+ ion in liquid samples of $\text{bmim}[\text{Cl}]$ ³⁷. They obtained two distinct crystals of then unknown crystal structures, which they called Crystal (1) and (2), and analyzed them by Raman spectroscopy. Each crystal exhibited a spectrum with distinct peaks at slightly different wavelengths, which the authors attribute to two distinct imidazolium ring structures. Bands at 625, 730, and 790 cm^{-1} were observed only for Crystal (1) and not for (2), and bands at 500, 600, and 700 cm^{-1} were observed only for Crystal (2) and not for (1). Interestingly, a superposition of these two spectra is seen in the Raman spectra of the $\text{bmim}[\text{Cl}]$ liquid (Figure 21). A similar spectrum is seen for liquid $\text{bmim}[\text{BF}_4]$, implying the simultaneous existence of these two cationic conformations in both liquid samples.

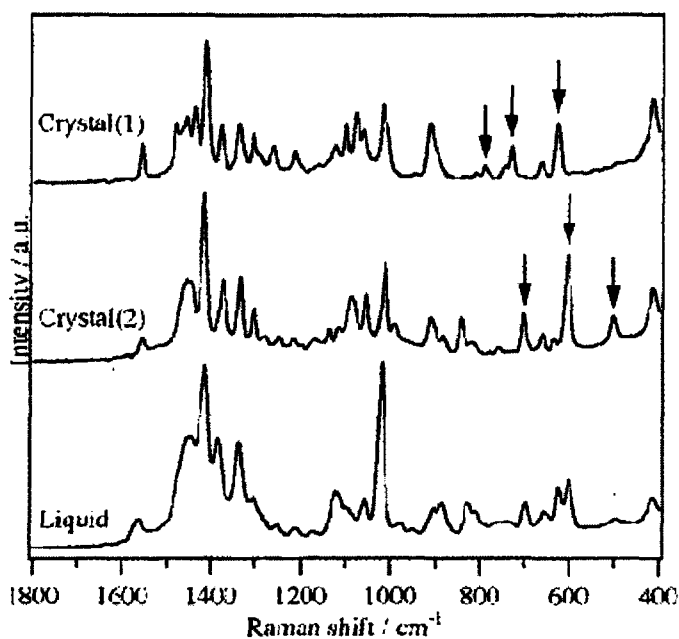


Figure 21 Raman spectra of the $\text{bmim}[\text{Cl}]$ polymorphs and supercooled liquid

Work by Adams, Fratini, Grossie and Dymek also suggests liquid state structure in an ionic liquid, ethyl-methylimidazolium chloride, by fourier transform infrared spectroscopy (FTIR). A superposition of the FTIR spectra of solid and liquid samples (Figure 22) demonstrates a strong similarity, leading the authors to conclude that “the interactions with Cl⁻ affecting the ring C-H stretches in emim⁺ are virtually the same in the solid and liquid phases of emim[Cl]”³⁴.

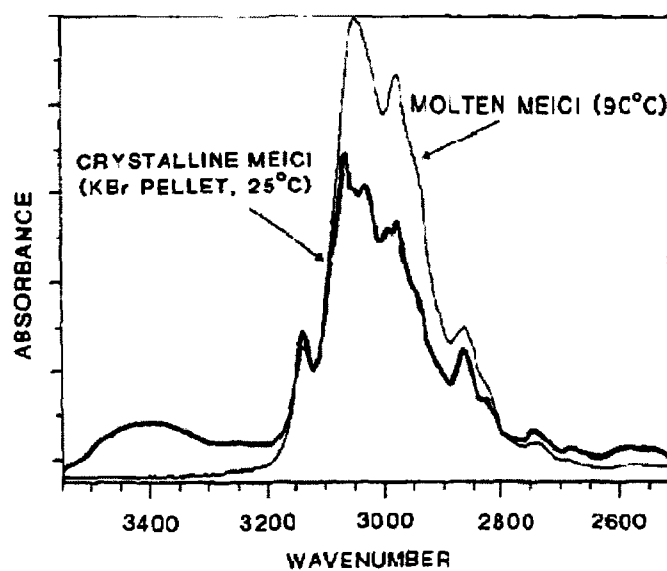


Figure 22 FTIR spectra of solid and liquid emim[Cl]

Katayanagi, Hayashi, Hamaguchi and Nishikawa studied bmim[I] by wide-angle X-ray scattering (WAXS) and Raman spectroscopy, reporting that the Raman spectrum of the liquid iodide salt agrees with the crystal and molten Raman spectra of the chloride and bromide salts, indicating that the cation structures in the liquids of the three bmim halides are similar to those in the crystals³⁸. The authors propose a model structure in

the liquid phase of bmim[I] that consists of four anions and one or more cations; they conclude that this structure is rigid enough to be observed by X-ray scattering from the liquid, and is “arranged in small crystal-like patches”, loosely aligned by hydrophobic interactions.

Chapter 4: Results and Discussion of IL Characterization

4.1 Differential Scanning Calorimetry

Samples analyzed by DSC in this study displayed varying degrees of supercooling; this is typical of ILs. Small changes in temperature ramp rates ($\pm 5^\circ/\text{min}$) can significantly alter observed melting and freezing points; higher rates can lead to severely broadened peaks and shift observed melting points by several degrees. This behaviour has been observed in great detail in bmim[Br] and bmim[Cl] by Nishikawa et al with their nano-Watt DSC³⁹. Rates used in the present study ranged from 1 to $5^\circ/\text{min}$ as appropriate to the sample and practical considerations. Typically a sample was heated from room temperature past its melting point, resting isothermally for 10 minutes prior to cooling. Once past the freezing point (which was not always observed) another 10-minute isotherm was employed prior to execution of another heating ramp; this procedure determined the repeatability of thermal behaviour. Emphasis was placed on obtaining a reasonably accurate determination of the melting point of the sample, in preparation for VTNMR studies; detailed studies of the thermal properties of ILs has been performed elsewhere with much greater attention paid to fine details³⁹⁻⁴¹.

Chlorides

Figure 23 shows the DSC plots for the chloride ILs. Each sample exhibits supercooling: a significant difference between their melting and freezing points, if the latter is observed at all. In Figure 23a) the ramp cycle of (heat to 170°C)-(hold for 10 min)-(cool to 10°C)-(hold for 10 min), with a ramp rate of $2^\circ\text{C}/\text{min}$, was repeated twice

for mbpyr[Cl]. The traces are almost entirely coincident, with a decrease of approximately 2°C in observed melting (155°C) and freezing (111°C) points. A similar result is observed in c) for emim[Cl], displaying a melting point at 90°C and freezing at 38°C. No freezing point was observed for bmim[Cl] and not surprisingly upon heating after one heat-cool cycle, a second melting curve was not observed; the first occurred at 71°C. In fact, the sample was allowed to sit at room temperature over 24 hours and still no melting point was observed upon heating (DSC not shown). A melting point was observed after allowing the sample to rest at -4°C over 48 hours (DSC not shown). This may be related to the frustration of crystallization into two available crystal structures, as reported by Holbrey et al ³⁵, and similar DSC results were obtained by Nishikawa et al ³⁹. Technical difficulties contributed to the absence of a freezing point in the DSC for bdmim[Cl] however the melting point was sufficiently characterized for our purposes at 99°C, and it is clear that there is significant supercooling, with at least a 70° difference between the melting and any potential freezing points at 1°C/min.

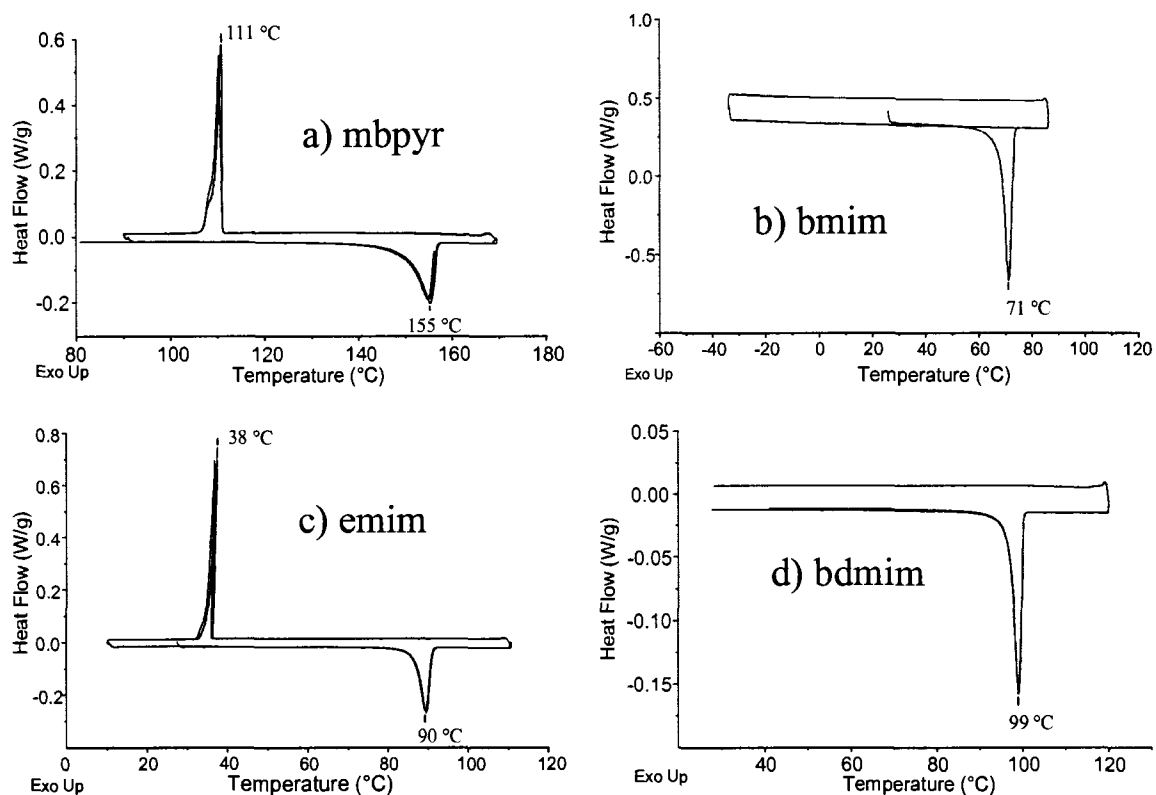


Figure 23 DSC plots for chloride ILs. Ramp rate = 2 °C/min for a)-c), 1 °C/min for d). All samples were heated from room temperature, and held at 10-minute isotherms before changing temperature ramp direction

Bromides and Iodides

With the exception of $\text{bNH}_3[\text{Br}]$, the bromides studied in this work have had their thermal characteristics previously investigated by other groups; the melting points from the literature were used for VTNMR work. As shown in Figure 24a), the difference between the melting (-23°C) and freezing (-30°C) points of $\text{bNH}_3[\text{Br}]$ is significantly smaller than those seen in the chlorides, however this can likely be attributed to a simpler cationic moiety and not to the anion. A reasonably large difference in melting (101°C) and freezing (82°C) points was observed in the DSC of $\text{dmpyrro}[\text{I}]$, shown in Figure 24c). This may be due in part to the ramp rate being relatively high at $5^\circ\text{C}/\text{min}$; a slower

run may narrow the observed gap. There is a significant amount of structure in the freezing peak; the origin of this structure is unknown and is left to future investigations. A narrow freezing/melting (46/48°C) difference was thought to have been observed in the DSC of tmim[I] (Figure 24b)). Upon further investigation, it was determined (by visual inspection) that the melting point of tmim[I] is in fact greater than 260°C. The peaks observed by DSC are attributed to a phase change. A large gap was again seen in the DSC of bdmim[I], with a melting point of 99°C and a freezing point of 44°C. This run, shown in Figure 24d), also used a ramp rate of 5°C/min.

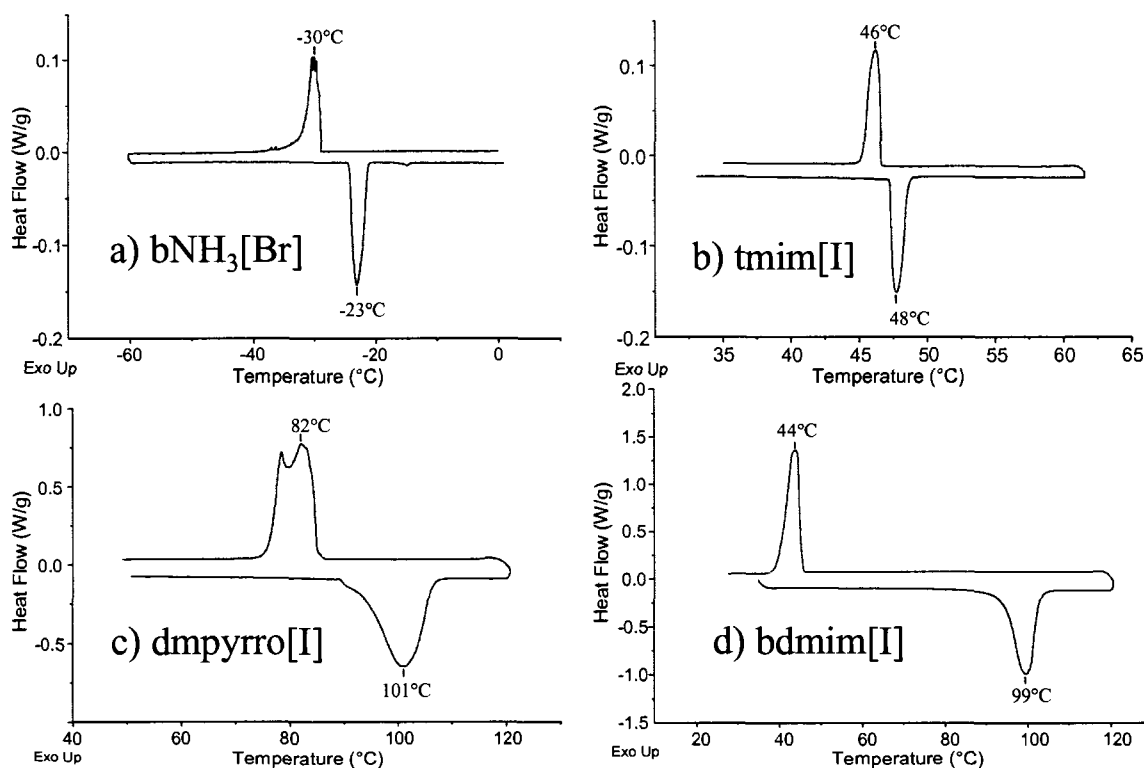


Figure 24 DSC plots for (a) bromide and (b),(c),(d) iodide ILs. Ramp rate = 1 °C/min for (a) and (b), 5 °C/min for (c) and (d). All samples were heated from room temperature, and held at 10-minute isotherms before changing temperature ramp direction

Summarized below in Table 1 are the melting points of those ILs here investigated by NMR, as established by DSC or as found in the literature.

Table 1 Melting points of studied ILs in °C

	Cl	Br	I
bmim	71	76 ^a	201.1 (±2.0) ^a
bdmim	100	-	99
emim	89	79 ^b	-
tmim	-	-	> 260
dmpyrro	-	-	100
empyrro	-	260 ^a	-
mbpyr	155	-	-
bNH₃	-	-23	-

*All values are from experimental work with an uncertainty of ± 2°C, except where noted: a) Merck, and b) Ngo et al (uncertainty not reported)

4.2 NMR Spectroscopy

Here the results of investigations by NMR spectroscopy are presented. ³⁵Cl, ⁷⁹Br and ¹²⁷I solid-state NMR (SSNMR) were employed to collect spectra and determine nuclear and CSA parameters of the anions by simulation. The evolution of these parameters (and so changes in the environment of the anions) was then observed by variable-temperature NMR (VTNMR). Correlations are illustrated between DSC data and VTNMR results for the chloride ILs. Liquid state NMR at different field strengths was employed to observe the local environment of the anions in molten ILs. T₁ and T₂ experiments were performed to further assess the degree of liquid-state structure. Finally

ab initio calculations were employed to simulate solid state nuclear and CSA parameters, which were then compared to experimentally obtained values.

4.2.1 Solid State NMR Results

For each solid sample, MAS sample spectra (if they could be obtained) were analyzed first to provide a CT center band line shape; this allowed for the unambiguous determination of C_Q , η_Q and the isotropic chemical shift. The static spectra of the samples were then analyzed with these parameters held fixed to determine their CS tensor parameters. Concurrent analysis of spectra acquired at both 21.15 T and 9.4 T allowed further refinement of the simulations. For a single spectrum multiple sets of parameters may each provide reasonable fits and so fitting spectra obtained at multiple field strengths with the same parameters is an essential test of the parameters' validity. Reported errors on the parameters were obtained by visual inspection of the deviation of the simulation from best fit.

This data established a baseline for the quadrupolar interactions of the anions in the solid state, a starting point for subsequent liquid-state NMR investigations. These are reported in Section 4.2.2.

Chloride IIs

The ^{35}Cl SSNMR spectra for the chloride salts, experimental and simulated, are shown in Figure 25. Experimentally determined quadrupolar and CS tensor parameters obtained by simulation of the acquired spectra are listed in Table 2. Isotropic chemical shifts are reported relative to 0.1 M NaCl in D_2O .

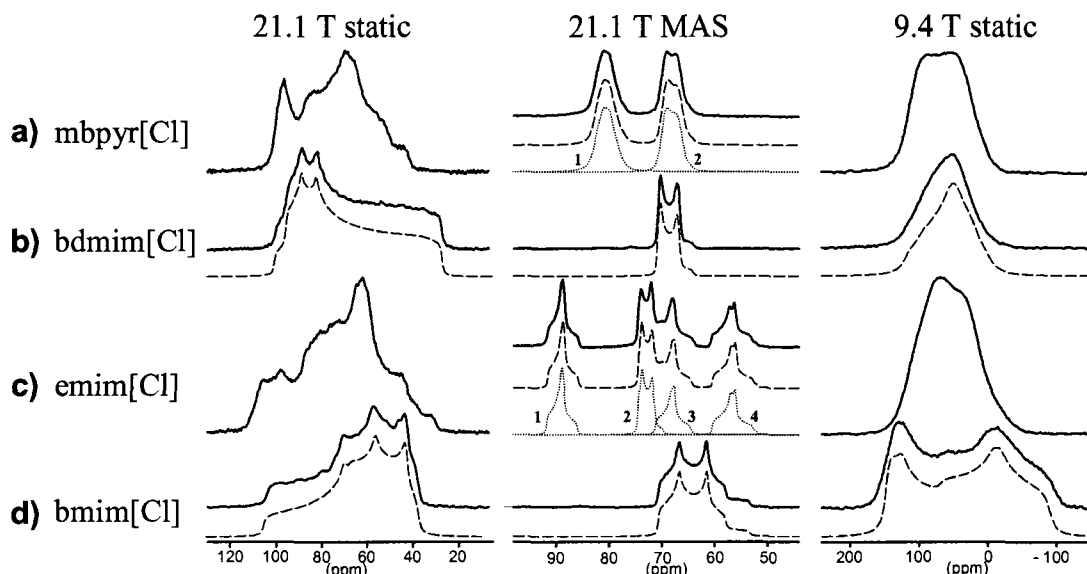


Figure 25 Experimental (solid lines) and simulated (dashed lines) SSNMR ^{35}Cl spectra.

The number of sites observed in each sample correspond with the crystal structures available for emim, bmim and bdmim[Cl]³⁴⁻³⁷ and obtained by X-ray diffraction for mbpyr[Cl]⁴². A complete set of CS tensor parameters and angles between tensors were found for the single-site samples; the multiple-site samples proved difficult to characterize satisfactorily due to overlapping lineshapes.

Table 2 ^{35}Cl experimental spectrum simulation fit parameters. Labelled parameters correspond to their respective numbered peaks in Figure 25

Cation		C_Q/MHz	η	δ_{iso}/ppm	Ω/ppm	κ	$\alpha/^\circ$	$\beta/^\circ$	$\gamma/^\circ$
mbpyri	1	0.857 ± 0.008	0.525 ± 0.005	83.15 ± 0.07	-	-	-	-	-
	2	0.889 ± 0.008	0.08 ± 0.08	70.56 ± 0.04	-	-	-	-	-
bdmim		0.978 ± 0.004	0.10 ± 0.02	71.60 ± 0.02	-47.4 ± 0.2	0.28 ± 0.01	16 ± 1	82.5 ± 0.5	-34 ± 4
	1	0.808 ± 0.004	0.95 ± 0.01	91.72 ± 0.03	-	-	-	-	-
emim	2	0.805 ± 0.005	0.20 ± 0.02	74.98 ± 0.04	-	-	-	-	-
	3	0.884 ± 0.004	0.86 ± 0.01	71.36 ± 0.04	-	-	-	-	-
	4	0.972 ± 0.005	0.80 ± 0.01	60.60 ± 0.03	-	-	-	-	-
bmim		1.500 ± 0.002	0.390 ± 0.005	71.65 ± 0.05	25.0 ± 0.5	0.48 ± 0.04	78 ± 2	76 ± 1	12 ± 2

The quadrupolar coupling constants ranged from 0.8 to 1.5 MHz and quadrupolar asymmetry parameters ranged from 0 to 0.95. Typical C_Q values for chloride ions in

organic and inorganic salts range from zero to greater than 9.0 MHz⁴³⁻⁴⁶. The CS tensor values are consistent with those found in other organic-chloride systems; Wasylishen reported δ_{iso} of 10-53 ppm for a series of five organic hydrochlorides⁴⁷ and Chapman reported 37-120 ppm for another series of ten organic hydrochlorides⁴³. Here a relatively narrow range of 61-92 ppm was observed. Spans in the same studies report a range of 45-150 ppm; spans of 44 and 78 ppm are reported here. These studies by Wasylishen and Bryce concerned hydrogen-bonded chlorides, and hydrogen bonding is generally regarded as an important interaction governing the structure and behaviour of imidazolium ionic liquids³⁴⁻³⁶. As mentioned in Section 3.2, at least one ab initio study has been performed in which the authors conclude that the bonding is “considerably different from that of conventional hydrogen bonds”³⁰. That being said, the Cl-H distances involved are similar to values typical of hydrogen bonding.

Bromide ILs

The ⁷⁹Br SSNMR spectra for the bromide salts, experimental and simulated, are shown in Figure 26. Experimentally determined quadrupolar and CS tensor parameters obtained by simulation of the acquired spectra are listed in Table 3. Isotropic chemical shifts are reported relative to 0.01 M NaBr in D₂O.

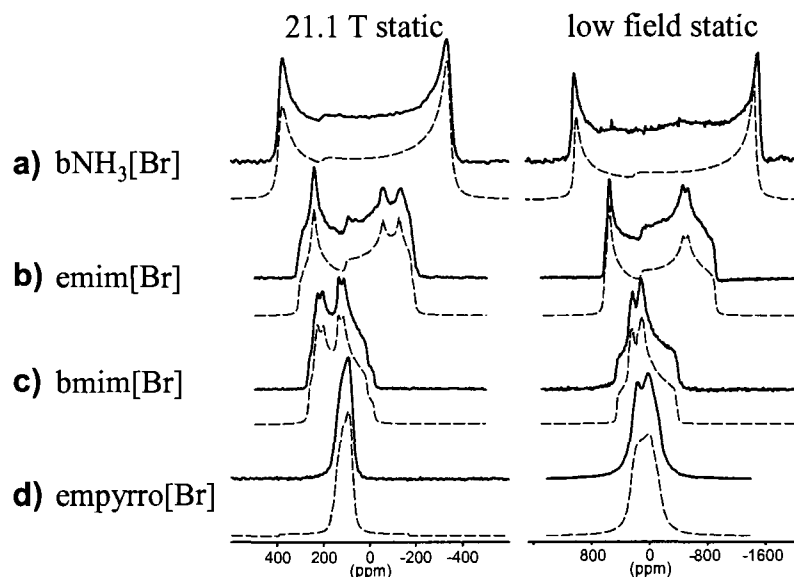


Figure 26 Experimental (solid lines) and simulated (dashed lines) SSNMR ^{79}Br spectra.

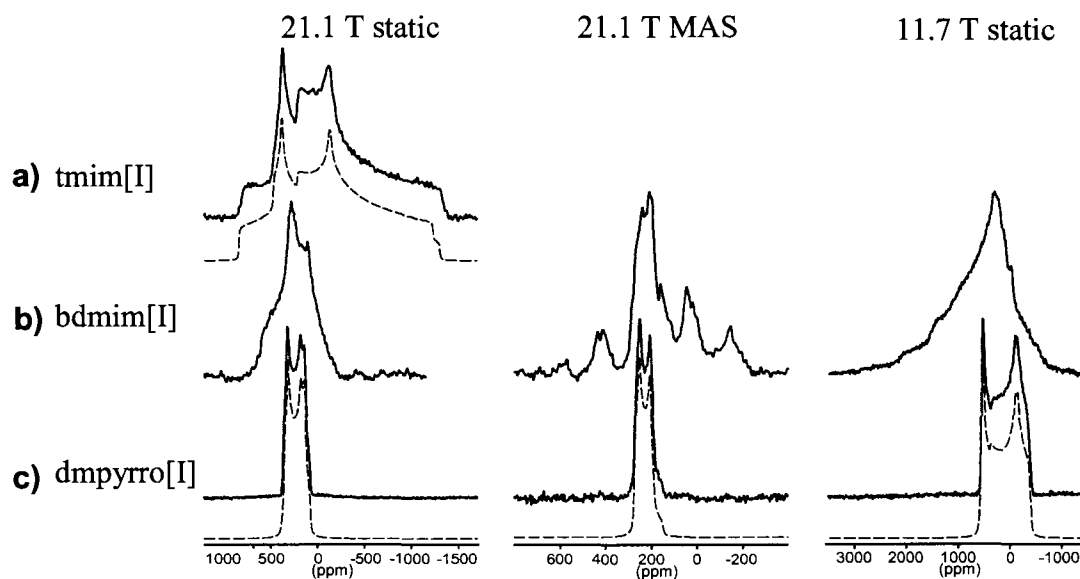
The ^{79}Br quadrupolar coupling constants covered a relatively large range, from 5.1 to 17.5 MHz, and quadrupolar asymmetry parameters ranged from zero to 0.86. There are far fewer SSNMR studies available for organic bromide systems than for organic chlorides, making comparisons difficult. The relatively large nuclear electric quadrupole moment of ^{79}Br leads to very large linewidths in systems that do not possess high symmetry and so most research has been restricted to high symmetry inorganic solids. The results obtained here are not out of line with those presented in a review of bromine-79/81 SSNMR⁴⁸. The number of sites observed in emim and bmim[Br] correspond to the crystal structures reported in the literature^{34, 35}.

Table 3 ^{79}Br experimental spectrum simulation fit parameters.

Cation ^a	C_Q/MHz	η	$\delta_{\text{iso}}/\text{ppm}$	Ω/ppm	κ	α° ^b	$\beta/^\circ$	$\gamma/^\circ$
BNH_3	17.50 ± 0.02	0.01 ± 0.01	137.0 ± 0.5	75 ± 2	0.05 ± 0.05	0	0	0
EMIM	12.40 ± 0.01	0.28 ± 0.01	122 ± 1	73 ± 3	0.95 ± 0.05	54 ± 3	81 ± 1	8 ± 2
BMIM	7.35 ± 0.05	0.86 ± 0.02	172 ± 1	-58 ± 2	0.64 ± 0.10	108 ± 3	18 ± 3	57 ± 3
EMPyrrO	5.12 ± 0.05	0.37 ± 0.08	123 ± 1	51 ± 1	0.96 ± 0.04	-83 ± 2	-21 ± 2	148 ± 2

Iodide ILs

The ^{127}I SSNMR spectra for the iodide salts, experimental and simulated, are shown in Figure 27. Experimentally determined quadrupolar and CS tensor parameters obtained by simulation of the acquired spectra are listed in Table 4. Isotropic chemical shifts are reported relative to 0.01 M KI in D_2O .

**Figure 27** Experimental (solid lines) and simulated (dashed lines) SSNMR ^{127}I spectra.

Only two iodide sample spectra were amenable to simulation, yielding quadrupolar constants of 17 MHz and 37 MHz and asymmetry parameters of 0.27 and 0.73. As with organic bromides, there are very few organic iodide SSNMR studies available for comparison. Again, the parameter values reported here are in line with those few presented in Bryce's review⁴⁸. No crystal structures were available for these ILs. The spectra for bdmim[I] suggest the presence of more than one site, however the signal was too broad to fully "spin out" the interactions and as a result spinning sidebands frustrated efforts to clarify the spectrum and extract parameters.

Table 4 ¹²⁷I experimental spectrum simulation fit parameters.

Cation	C_Q /MHz	η	δ_{iso} /ppm	Ω /ppm	κ	$\alpha/^\circ$	$\beta/^\circ$	$\gamma/^\circ$
trimim	36.8 ± 0.9	0.73 ± 0.01	143 ± 18	0	0	-	-	-
mmpyrro	16.9 ± 0.1	0.27 ± 0.02	282.0 ± 0.7	184 ± 3	-0.20 ± 0.05	56 ± 7	13 ± 2	31 ± 5

4.2.2 Liquid State NMR Results

Chloride ILs

The liquid state NMR spectra for the chloride samples are presented in Figure 28. Acquisition parameters can be found in Section 8.3 of the Appendix. Simple isotropic lineshapes were observed. Spectra were acquired at multiple field strengths, 9.4 T and 4.7 T, to test for the presence of second order quadrupolar effects which would indicate the presence of some structural elements. No significant difference, either in isotropic shift or in linewidth, was observed.

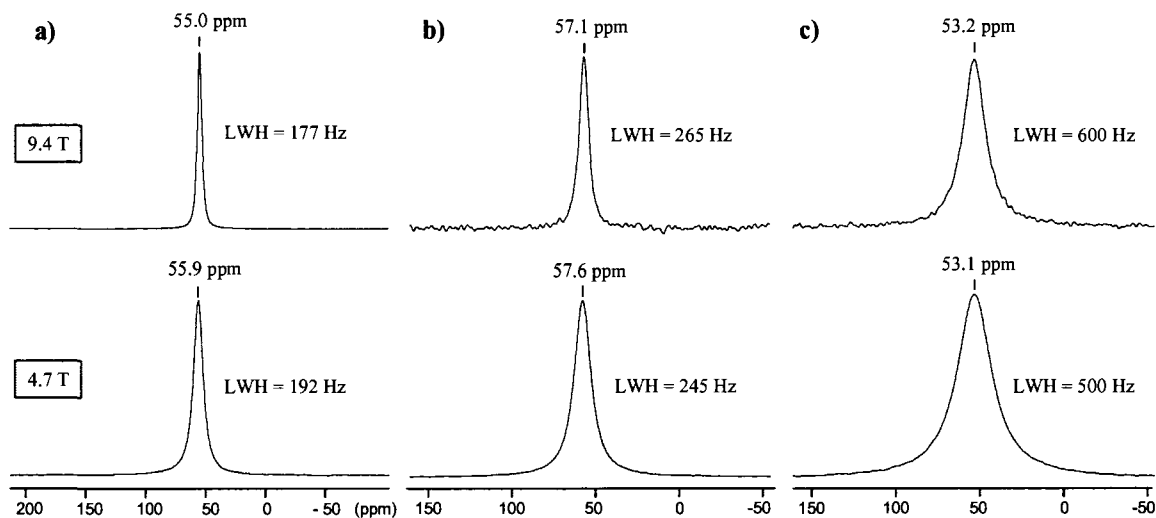


Figure 28 Liquid-state ^{35}Cl spectra for a) emim, b) bmim and c) bdmim chlorides at 9.4 T (upper) and 4.7 T (lower).

The transition from solid to liquid state was observed by stepwise VTNMR; temperature was increased from room temperature and held at the target temperature for at least ten minutes prior to acquisition to allow the sample ample time to equilibrate. Acquisition times were on the order of 30 minutes. The progression from solid to liquid state is illustrated in Figure 29, Figure 30 and Figure 31 for emim, bmim and bdmim[Cl] respectively; the spectra are aligned with the appropriate region in the DSC of the sample (acquired separately from the spectra). Examination of the spectra for emim and bmim[Cl] show evidence of partial melting prior to observation of isotropic peaks; the isotropic peak can be seen “growing” out of the solid lineshape. The spectra for bdmim[Cl] show a sharp transition from solid lineshape to isotropic liquid peak over a 5°C increase. In each series the solid lineshape is observed to disappear abruptly and entirely.

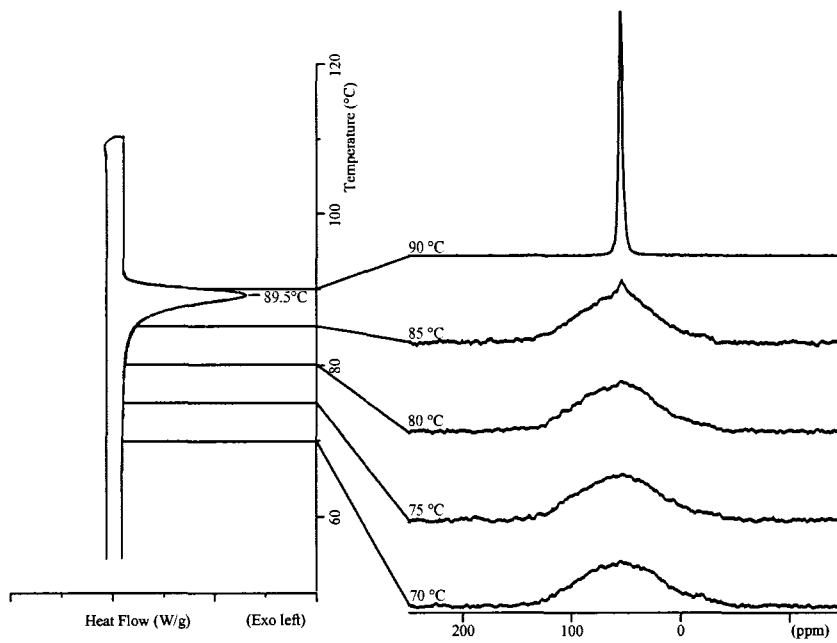


Figure 29 DSC profile with NMR spectra at 9.4 T for emim[Cl]

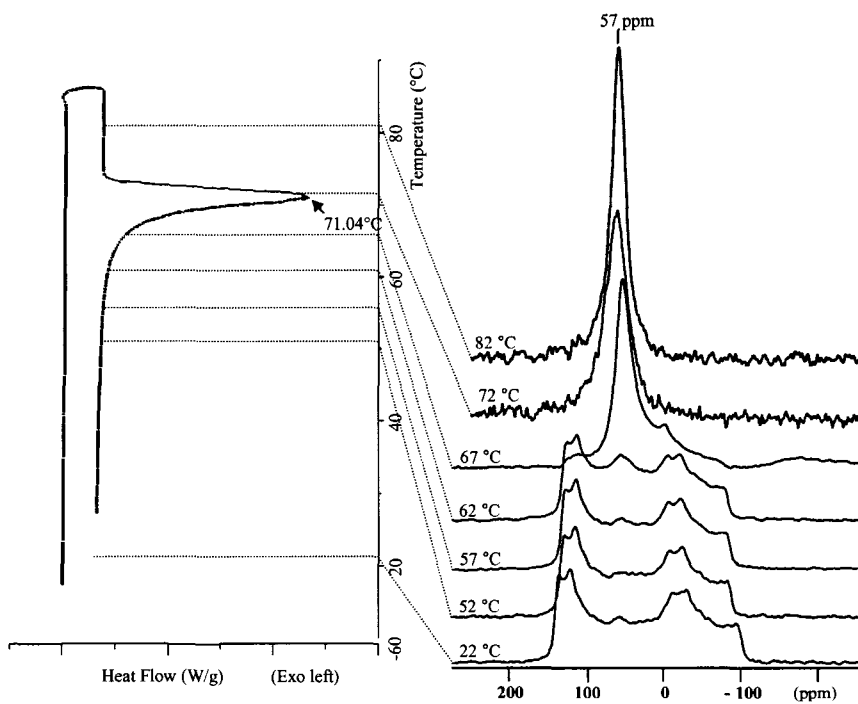


Figure 30 DSC profile with NMR spectra at 9.4 T for bmim[Cl]

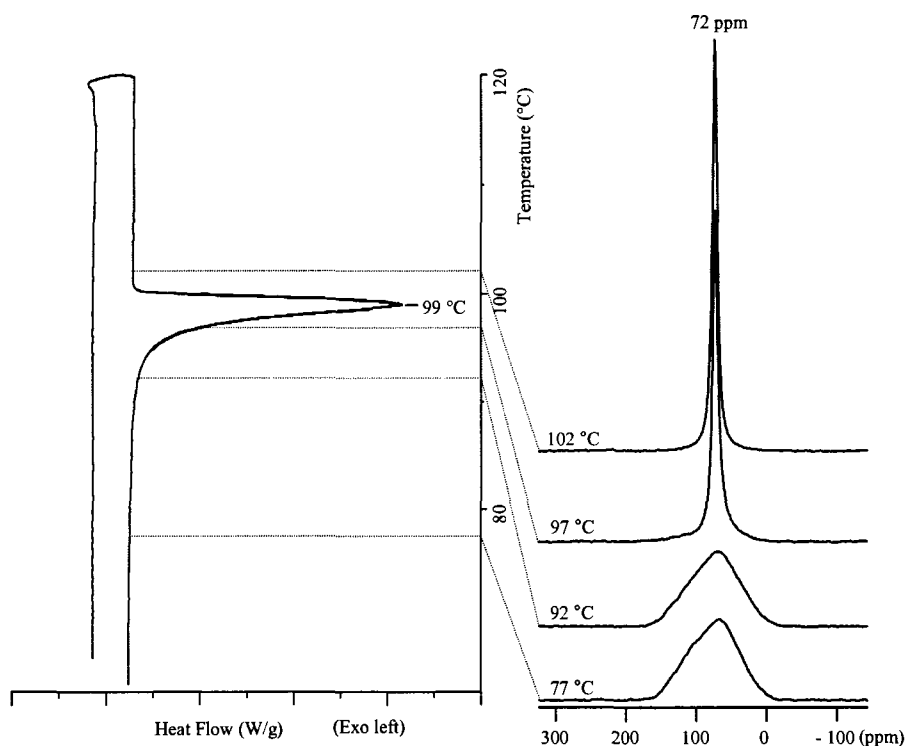


Figure 31 DSC profile with NMR spectra at 9.4 T for bdmim[Cl]

Figure 32 stacks the liquid state ^{35}Cl spectra acquired from a bmim[Cl] sample as it was cooled. The temperature ramping employed followed the procedure reported by Hayashi et al in their Raman work, described in Section 3.5. They reported an increase in the intensity of Raman bands attributed to a specific conformation of the bmim cation, concluding that some local structure exists in the liquid state. The NMR spectra reported here show line broadening with decreased temperature and a decrease in signal strength; both of these are expected as a sample is cooled and viscosity increases, but neither observation provides conclusive support for the local structure model.

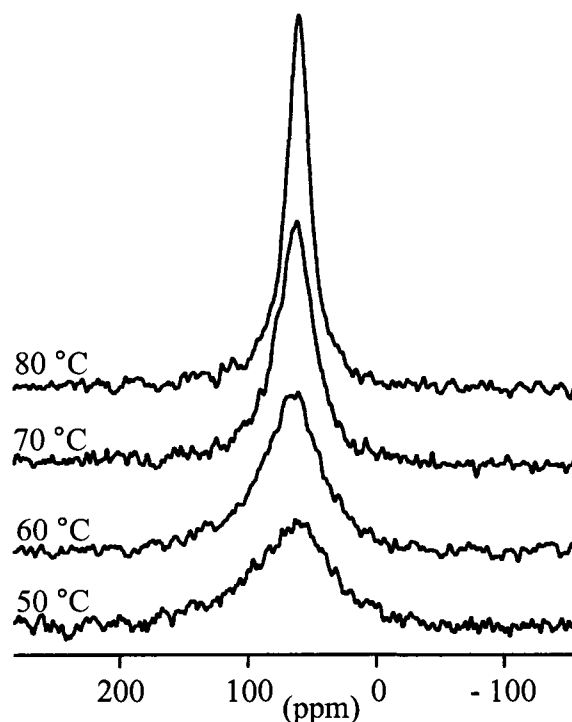


Figure 32 ^{35}Cl VTNMR at 9.4 T of $\text{bmim}[\text{Cl}]$, cooled from 80°C to 50°C

Bromide ILs

The liquid state NMR spectra for two bromide samples, emim and bmim[Br], are presented in Figure 33. The molten spectra of bNH₃[Br] was not acquired due to moisture contamination of the sample and time constraints. Results similar to those obtained from the chloride samples were observed. As for the other samples, the ^{79}Br signal from molten bdmim[Br] was not seen and is speculated to be too broad to be acquired, and the melting temperature of mbpyr[Br] is not obtainable with the available VTNMR apparatus. Acquisition parameters can be found in Section 8.3 of the Appendix. Simple isotropic lineshapes were again observed. As with the chlorides, spectra were acquired at multiple field strengths, 9.4 T and 4.7 T, to test for the presence of second order quadrupolar effects. No significant difference, either in isotropic shift or in

linewidth was observed for emim[Br]. The spectra collected from liquid [bmim]Br samples do appear to show some significant differences in both isotropic shift and linewidth, however the shift observed is opposite in direction to that expected from second order quadrupolar interaction effects. It is proposed that the differences seen here stem from approaching the experimental limits of the equipment used; the breadth of the sweep width necessary to acquire the spectrum at 4.7 T introduced distortions in the spectrum that rendered accurate phasing problematic. This view is supported by investigations of T_1 and T_2 relaxation times reported below, which also provide no evidence for local structure.

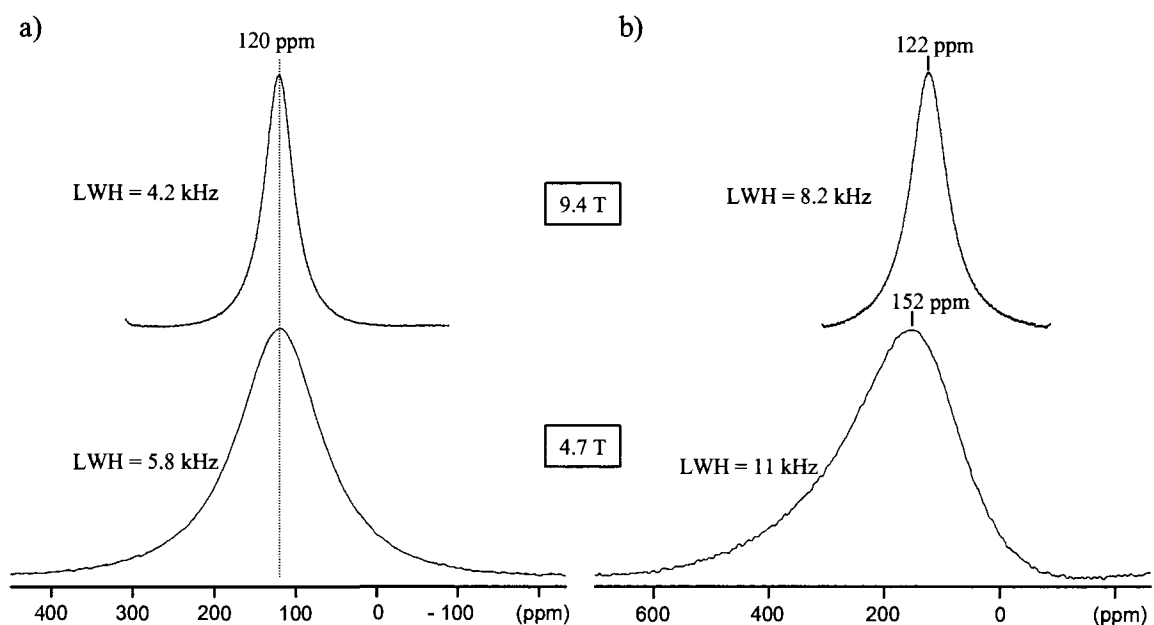


Figure 33 Liquid-state ^{79}Br spectra for a) emim and b) bmim bromides at 9.4 T (upper) and 4.7 T (lower).

Relaxation Time Experiments

T_1 and T_2 measurements of molten samples were performed to evaluate the nature of the local structure, if any, of the ILs. As described in Section 2.3.5, the ratio T_1/T_2 near the melting point of a sample can be helpful in this regard: a large ratio results from strong interactions indicative of local structure while a ratio of one (1) indicates an isotropic liquid. Intermediate values close to unity are typical of viscous liquids, where the ratio increases with increasing viscosity. Experimental results are illustrated in Figure 34 and Figure 35 for the chlorides and bromides respectively, using the same format as the theoretical example given in Figure 20.

As with VTNMR experiments reported above, samples were allowed to equilibrate at the target temperature for at least ten minutes prior to acquisition. Each sample was heated from 20 to 40°C above its melting point, and then cooled. In Figure 34a), the emim[Cl] was observed to transition from a isotropic liquid to a solid. In the liquid regime the ratio averages 1.88 ± 0.10 . For bmim and bdmim[Cl] the solid regime is not included. An average T_1/T_2 ratio of 2.63 ± 0.12 was observed for bmim[Cl], 2.93 ± 0.13 for bdmim[Cl], 1.26 ± 0.13 for emim[Br] and 1.07 ± 0.08 for bmim[Br]. Experimental data is provided in Section 8.2 of the Appendix.

These ratios are all consistent with a liquid of low viscosity. In such a sample, there are molecular motions that correspond to correlation times on the scale of the Larmor frequency of the nucleus under study (39.2 MHz for ^{35}Cl and 100.2 MHz for ^{79}Br) which reduces the value of T_1 , as well as some slightly slower molecular motions which are responsible for a further reduction in the T_2 constant. The observed ratios are not high enough to suggest sustained order in the liquid state.

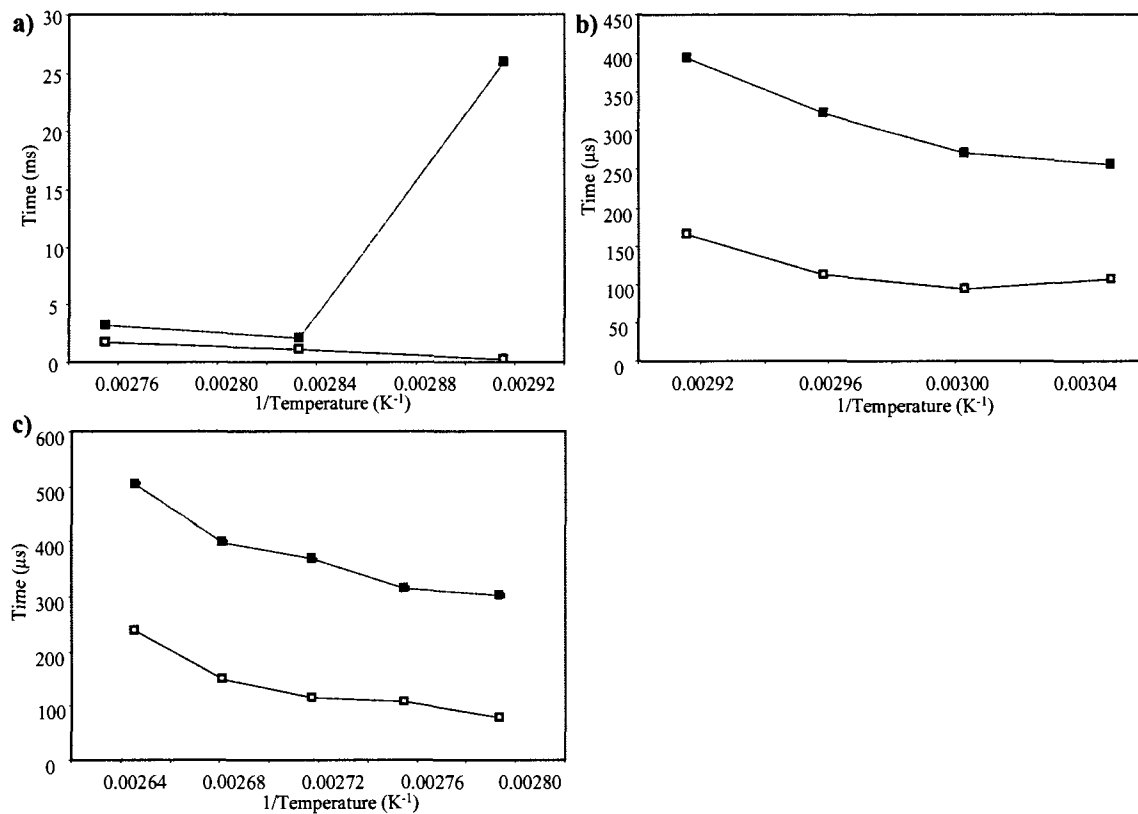


Figure 34 Relaxation times for a) emim, b) bmim and c) bdmim chlorides. Closed squares represent T_1 values and open squares represent T_2 values.

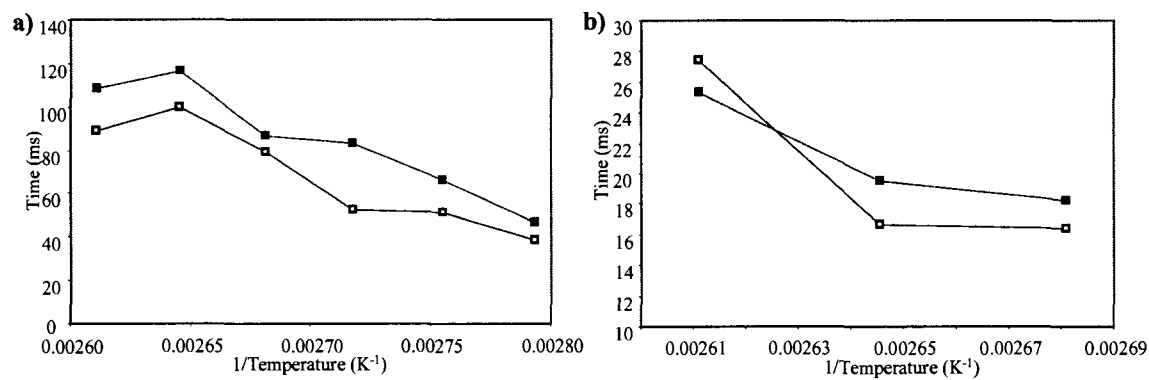


Figure 35 Relaxation times for a) emim and b) bmim bromides. Closed squares represent T_1 values and open squares T_2 values.

4.2.3 Gaussian Calculations

In order to compare experimentally obtained values with theory, *ab initio* calculations of ^{35}Cl quadrupolar and chemical shift anisotropy interactions were performed; the heavier anions are not amenable to this method. Examples of the input files used are provided in Section 8.4 of the Appendix and the procedure is outlined in detail in Section 6.3.5. The resulting parameters are tabulated along with their experimental counterparts in Table 5.

Table 5 ^{35}Cl nuclear quadrupole and CSA parameters calculated by Gaussian 98 (G98), and experimental data. Monoclinic bmim values marked by *; not observed experimentally.

Cation	C_Q G98	C_Q	η G98	η	d_{iso} G98	d_{iso}	Ω G98	Ω	κ G98	κ
emim	-0.814	0.888	0.84	0.87	56.7	71.4	61.2	-	-0.45	-
	-2.572	0.808	0.69	0.93	93.7	91.7	67.8	-	-0.71	-
	-1.136	0.807	0.61	0.23	78.9	75	84.7	-	-0.03	-
	1.122	0.977	0.83	0.8	50.8	60.6	40.2	-	-0.26	-
bmim	-2.370	1.495	0.52	0.39	59.2	71.5	51.9	41.8	0.606	-0.448
	-2.835*	-	0.41*	-	56.3*	-	46.3*	-	0.465*	-
bdmim	1.336	0.978	0.92	0.11	63.7	71.6	71.4	77.7	-0.524	0.659
mbpyr	1.365	0.889	0.48	0.13	55.6	70.6	39.3	-	-0.311	-
	1.101	0.857	0.82	0.52	83.9	83.1	41.2	-	-0.468	-

Reasonable agreement with respect to the quadrupolar coupling constant and isotropic shifts were obtained, with the significant exception of one site in emim[Cl]. The C_Q 's of the other IL sites were reproduced within 37%, with an average error of 22%, excluding that of emim[Cl] which the calculation overestimated by 69% (note that experiment cannot determine the sign of C_Q). These errors are slightly higher than those reported using the same basis sets by Chapman and Bryce on organic chloride systems (<12%)⁴³. It is likely that the pruning technique employed in this work to reduce atom

counts (also described in Section 6.3.5) is responsible for these errors, as it made unavoidable changes to bonding and hence electron distribution; this was necessary to ensure timely results. It would be reasonable to assume that removing nearby chlorides might also have an impact on C_Q calculations, however the first two nuclei listed in Table 5 each have a chloride within 5.240 Å and each calculation gives a significantly different error of 9 and 69%. The next largest error (37%) is seen for bmim[Cl], whose smallest Cl-Cl distance is 4.7 Å. A comparison of theoretical and experimental values is illustrated in Figure 36.

Better agreement was obtained between the experimental and calculated isotropic chemical shifts; all were within 27% with an average of 14% deviation. In the same paper mentioned above, Chapman and Bryce reported an underestimation of the isotropic shift in all but one of the systems studied. In the present work five shifts were underestimated and three were overestimated by theory. The obtained values for the chemical shift spans were in good agreement, but with only two experimental values for comparison a trend cannot be assumed.

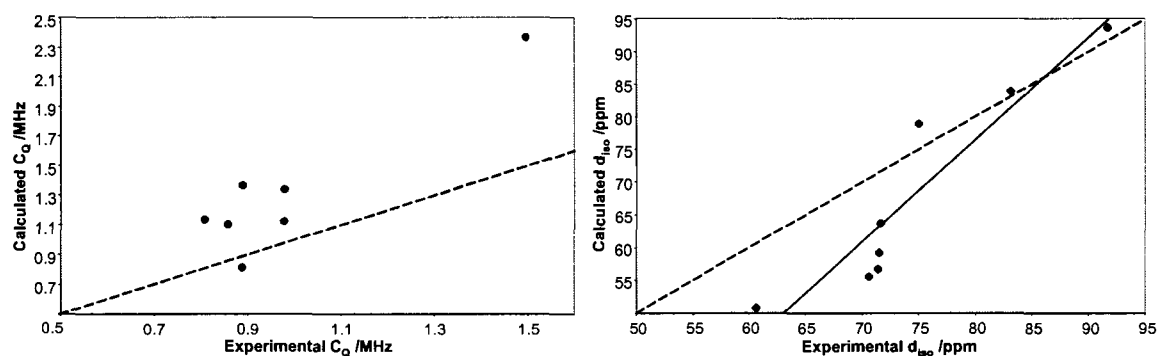


Figure 36 Comparison of parameters calculated with Gaussian 98 and experimental data. Dashed line represents best-case scenario of Calculated = Experimental. The equation for the line of best fit (solid line in right chart) is $y = 1.5616x - 48.428$, with an R-value of 0.8659.

Chapter 5: Conclusions

The environment of halides in a selection of ionic liquids was investigated experimentally by NMR spectroscopy and theoretically. It was discovered that for chloride, bromide and iodide ILs in the solid state, the quadrupolar and chemical shift interactions of the halide nucleus are consistent with those found in other solid organic chloride, bromide and iodide salts. Theoretical simulation of the tensors showed reasonable agreement with experimental findings.

The presence of long-range order in halide ionic liquids in the liquid state was investigated experimentally by variable-temperature NMR spectroscopy. Relaxation time experiments showed that the liquid ILs studied have very similar T_1 and T_2 relaxation constants near their melting points, demonstrating that they behave very much as typical liquids, demonstrating a lack of evidence for any significant order other than that found in isotropic liquids. A comparative study of spectra acquired at multiple field strengths revealed that residual second-order quadrupolar effects were absent, further demonstrating a lack of significant order on a timescale of $\sim 10^{-3}$ sec. The results suggest that reports in the literature of observed “structure” must exist on a shorter timescale as indeed these have been found by techniques such as FTIR, Raman spectroscopy and ab initio simulation and therefore are too short-lived to constitute “long-range order” in molten ionic liquids on the timescales probed by NMR in this work.

To further explore this question it may be possible using NMR spectroscopy and isotopic doping of the cations to evaluate any tendencies for the anions to remain associated with specific sites on the cation in the liquid state. The relative ease of synthesis of ionic liquids recommends this approach.

Chapter 6: Experimental Details

All ionic liquids were supplied by EMD Chemicals except for bmim[Cl] which was supplied by Strem Chemicals and bNH₃[Br] which made by standard metathesis techniques from n-butyl-bromide and an amine.

6.1 Preparation of Samples

Samples were lightly ground, packed and sealed into sample tubes under argon since very low concentrations of water can significantly alter IL properties⁴⁹. bNH₃[Br] samples were synthesized and prepared in air and so there may be some water contamination in these samples; the extent of which was not characterized. Sample sizes included 4mm o.d. ceramic MAS rotors on the 900MHz spectrometer, 7mm o.d. ceramic MAS rotors on the 200MHz, and 5mm glass tubes cut to appropriate length for static spectra on the 400 MHz spectrometer.

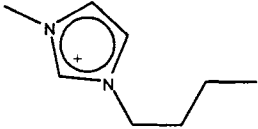
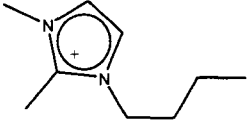
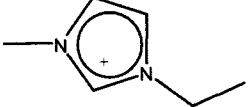
6.1.1 Reference Samples

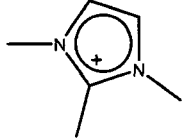
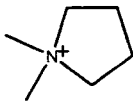
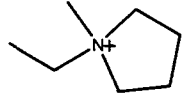
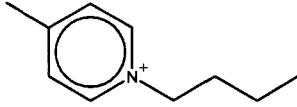
The following IUPAC-recommended chemical shift references were employed: 0.1 M solution of NaCl, a 0.01 M solution of NaBr, and 0.01 M solution of KI (all in D₂O) for chlorine, bromine, and iodine, respectively⁵⁰. To establish 'solid' central-transition $\pi/2$ pulse lengths for solid IL samples, powdered and/or saturated solution samples of NaCl, KBr, NaBr, KI and NaI were used, as appropriate.

6.1.2 Ionic Liquid Samples

Ionic liquids were selected for study based primarily on their relevance to existing work; for example, imidazolium cations are widespread in IL studies and development. ILs were selected for a variety of alkyl groups for a given anion, such as bmim, emim and bdmim[Cl] and also for a variety of anions for a given cation, such as bmim[Cl, Br or I], to allow for interesting direct comparisons. An additional matter was availability; ILs are fairly straightforward to synthesize, but the focus of this work was to establish a reasonably broad survey and so all ILs, with the exception of bNH₃[Br], were purchased from suppliers to leave more time for experiment and analysis. This also allowed for peace of mind with respect to moisture contamination; the ILs were delivered in bottles sealed under argon, then transferred to an argon dry-box for sample preparation. A summary with abbreviations and structures is given in Table 6.

Table 6 Cations, their structures and abbreviations. Also shown are the anion pairs for a given cation investigated in this work.

Abbreviation	Full name	Structure
bmim [Cl,Br,I]	1-butyl-3-methyl imidazolium	
bdmim [Cl,I]	1-butyl-2,3-dimethyl imidazolium	
emim [Cl,Br]	1-ethyl-3-methyl imidazolium	

tmim [I]	1,2,3-trimethyl imidazolium	
dmpyrro [I]	1,1-dimethyl pyrrolidinium	
empyrro [Br]	1,1-ethylmethyl pyrrolidinium	
mbpyr [Cl]	1-butyl-4-methyl pyridinium	
bNH ₃ [Br]	n-butyl amine	

6.2 Solid and Liquid State NMR

6.2.1 NMR Spectrometers and Probes

Solid-state NMR experiments were carried out with the following: a Bruker AVANCE-II 900 MHz NMR spectrometer operating at a magnetic field of 21.1 T (Larmor frequencies: 88.19 MHz for ³⁵Cl, 225.52 MHz for ⁷⁹Br and 180.09 MHz for ¹²⁷I) using a standard-bore double-resonance 4 mm MAS NMR probe; a Tecmag 500 MHz NMR spectrometer operating at a magnetic field of 11.74 T (Larmor frequencies: 49.00 MHz for ³⁵Cl, 125.3 MHz for ⁷⁹Br and 100.06 MHz for ¹²⁷I) using a homemade standard-bore single-resonance 5 mm static NMR probe; a Bruker AVANCE 400 MHz NMR spectrometer operating at a magnetic field of 9.39 T (Larmor frequencies: 39.19 MHz for

^{35}Cl , 100.21 MHz for ^{79}Br and 80.03 MHz for ^{127}I) using a Morris Instruments wide-bore double-resonance 7 mm static NMR probe; and a Bruker AVANCE 200 MHz NMR spectrometer operating at a magnetic field of 4.7 T (Larmor frequencies: 19.60 MHz for ^{35}Cl , 50.12 MHz for ^{79}Br and 40.02 MHz for ^{127}I) using a Bruker wide-bore double-resonance 7 mm MAS NMR probe.

6.2.2 Magic Angle Spinning (MAS)

All MAS experiments were performed at ambient temperature. No corrections were made with respect to sample heating under MAS conditions; the DSC data established with reasonable certainty that the heat generated would not have a significant impact on crystal structure. This assumption was borne out by correlation with static sample spectra; no changes in the quadrupolar tensor were observed. When necessary, the magic angle was set by standard procedure using the ^{79}Br signal from a solid powdered KBr sample: the angle is adjusted such that there are as many and as intensive rotational echoes as possible in the FID.

6.2.3 Variable Temperature NMR (VTNMR)

In all VTNMR experiments, the temperature was increased by 10°C intervals to the desired temperature where it was allowed to sit for at least 10 minutes prior to initiating the pulse sequence. A thermocouple positioned close (within 1 cm) to the sample monitored the temperature; any deviation from the true sample temperature was considered insignificant. Heat was generated by a resistive coil under computer control and delivered by nitrogen gas flow to the sample stage area of the probe. Probe tuning

and matching was performed at each temperature; significant drift was observed as the coil and capacitors in the resonance circuit were heated along with the sample.

6.3 Computer simulation

Computational methods were used to calculate the quadrupolar coupling constant, asymmetry parameter, isotropic chemical shift, span and skew. All calculations were performed using the Gaussian-98 program in the following manner: A cluster of atoms for simulation was chosen from the crystal structure; a central chlorine atom surrounded by its cationic neighbours, limited to those that have at least one atom within a roughly 6 Å radius of the chlorine nucleus. To strike a balance between expedient simulation and accuracy, the number of atoms to be simulated was further reduced by “pruning” sections of cations outside of the 6 Å radius and then capping the resulting dangling bonds with hydrogen atoms as appropriate. For example, if a bmim cation was oriented such that its butyl group was pointing at the chlorine atom and the imidazole ring was on the far side, the ring might be removed and the butyl group capped such that it becomes butane as illustrated in the cartoon below. (Note that for the simulation the chlorine atom would be surrounded by up to nine cations)

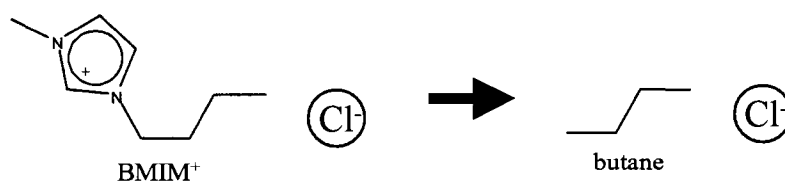


Figure 37 Pruning distant atoms to simplify Gaussian calculations

Once a satisfactory cluster was assembled, a Hartree-Fock (HF) calculation with the basis set STO-3G was used to quickly and roughly determine proton positions (which

it should be noted are not determined to any significant degree of accuracy by x-ray diffraction methods; they are often placed “by hand” once the positions of the heavier atoms have been determined). STO-3G is a minimal basis set of Slater-Type-Orbitals simulated by the sum of three Gaussian functions. To further refine the proton positions a second HF calculation was performed with the 6-31G basis set, which is a Pople split-valence double-zeta basis set where six primitive Gaussians comprise each core atomic orbital basis function and the valence orbitals are composed of two basis functions each; one composed of a linear combination of three primitive Gaussian functions, the other composed of one such function. Optimizing proton positions using only the 6-31G basis set is also a viable option but risks being much slower than this two-step method.

The proton positions determined from the HF/STO-3G and 6-31G calculations were then used with the crystal structure data to calculate the NMR parameters for the chlorine nuclei following a method outlined by Chapman and Bryce⁴³. The EFG tensors were determined using a Hartree-Fock calculation with the Dunning type cc-pVTZ basis set for the chloride ion and the cc-pVDZ basis set for all other atoms. Shielding tensor parameters were calculated using a hybrid B3LYP DFT method with a basis set of aug-cc-pVDZ for chlorine and cc-pVDZ for all other atoms.

The EFG tensors reported in the Gaussian output files were analyzed using the EFGShield program developed by Adiga, Aebi and Bryce⁵¹. EFGShield takes the G98 output file as input, asks the user to identify the atom of interest and then automatically parses the G98 output to find the full EFG and shielding tensors for that atom, as well as the Euler angles relating the orientations of the tensors' principal axis systems. The

principal components of the shielding tensors provided by Gaussian were converted to the convention described in Section 2.2.

6.3 Differential Scanning Calorimetry

A TA Instruments DSC2920 Modulated DSC calorimeter with N₂ purge gas and liquid nitrogen connection for cooling was used to characterize the thermal behaviour of the ILs. This was done to establish appropriate target temperatures as well as establishing heating and cooling rate response for subsequent variable-temperature NMR (VTNMR) experiments. Sample sizes ranged from 5 to 25 mg. Samples were sealed in aluminum pans and the system was calibrated with a mercury standard.

Thermal Solutions is a software program designed to operate the TA Instruments thermal analysis equipment, and was used to run the experiments and collect the data. The data was analyzed and plotted using the TA Instruments software *Universal Analysis*.

Chapter 7: References

1. Schurko, R. W. Introduction to Solid State NMR.
2. Wu, G. & Dong, S. High-Field ^{127}I NMR of Solid Sheelite Structures: Periodates Revisited. *Solid State Nuclear Magnetic Resonance* **20**, 100 (2001).
3. Walden, P. *Bull. Acad. Sci. St. Petersburg*, 405 (1914).
4. Weingärtner, H. Understanding Ionic Liquids at the Molecular Level: Facts, Problems, and Controversies. *Angew. Chem. Int. Ed.* **47**, 654 (2008).
5. Borisov, S. M., Waldhier, M. C., Klimant, I. & Wolfbeis, O. S. Optical Carbon Dioxide Sensors Based on Silicone-Encapsulated Room-Temperature Ionic Liquids. *Chem. Mater.* **19**, 6187-6188-6194 (2007).
6. Pârvulescu, V. I. & Hardacre, C. Catalysis in Ionic Liquids. *Chem. Rev.* **107**, 2615-2616-2665 (2007).
7. van Rantwijk, F. & Sheldon, R. A. Biocatalysis in Ionic Liquids. *Chem. Rev.* **107**, 2757-2758-2785 (2007).
8. Pushparaj, V. L. *et al.* Flexible energy storage devices based on nanocomposite paper. *PNAS* **104**, 13574-13575-13577 (2007).
9. Sathish, M. & Miyazawa, K. Size-Tunable Hexagonal Fullerene (C₆₀) Nanosheets at the Liquid-Liquid Interface. *J. Am. Chem. Soc.* **129**, 13816-13817 (2007).
10. Xu, L., Choi, E. & Kwon, Y. Ionothermal Syntheses of Six Three-Dimensional Zinc Metal-Organic Frameworks with 1-Alkyl-3-methylimidazolium Bromide Ionic Liquids as Solvents. *Inorg. Chem.* **46**, 10670-10671-10680 (2007).
11. Facey, G. CHM 4380 / 8309B Practical NMR Spectroscopy Class Notes. (2008).
12. Levitt, M. H. in *Spin dynamics : basics of nuclear magnetic resonance* (John Wiley & Sons, Chichester ; New York :, 2001.).
13. Duer, M. J. in *Introduction to solid-state NMR spectroscopy* (Blackwell Publishing Ltd., Oxford, UK, 2004).
14. Duer, M. J. *Solid-State NMR Spectroscopy Principles and Applications.* (2002).
15. Mehring, M. in *Principles of High Resolution NMR in Solids* (Springer-Verlag, Berlin, 1983).
16. Fyfe, C. A. in *Solid State NMR for Chemists* (C.F.C. Press, P.O. Box 1720, Guelph, Ontario, Canada, N1H 3V1, 1983).

17. Farrar, T. C. & Becker, E. D. in *Pulse and Fourier Transform NMR: Introduction to Theory and Methods* (Academic Press, New York and London, 1971).
18. Massiot, D. *et al.* *Modelling one and two-dimensional solid-state NMR spectra.* *Mag. Res. Chem.* **40**, 70-71-76 (2002).
19. Amoureux, J.
20. M. J. Frisch *et al.* Gaussian 98, Revision A.11.3. (2002).
21. Giernoth, R. & Bankmann, D. Magnetic resonance spectroscopy in ionic liquids. *Prog. NMR Spec.* **51**, 63 (2007).
22. Welton, T., Seddon, K. R., Day, M. P., Chaloner, P. A. & Avent, A. G. Evidence for Hydrogen Bonding in Solutions of 1-Ethyl-3-methylimidazolium Halides, and its Implications for Room-temperature Halogenaluminatate(III) Ionic Liquids. *J. Chem. Soc. Dalton Trans.*, 3405 (1994).
23. Antony, J. H., Mertens, D., Dölle, A., Wasserscheid, P. & Carper, W. R. Molecular Reorientational Dynamics of the Neat Ionic Liquid 1-Butyl-3-methylimidazolium Hexafluorophosphate by Measurement of ^{13}C Nuclear Magnetic Relaxation Data. *ChemPhysChem* **4**, 588 (2003).
24. Bagno, A., D'Amico, F. & Saielli, G. Computing the NMR Spectrum of a Bulk Ionic Liquid Phase by QM/MM Methods. *J. Phys. Chem. B* **110**, 23004 (2006).
25. Del Pópolo, M. G., Lynden-Bell, R. M. & Kohanoff, J. Ab Initio Molecular Dynamics Simulation of Room Temperature Ionic Liquid. *J. Phys. Chem. B* **109**, 5895 (2005).
26. Katsyuba, S. A., Dyson, P. J., Vandyukova, E. E., Chernova, A. V. & Vidiš, A. Molecular Structure, Vibrational Spectra, and Hydrogen Bonding of the Ionic Liquid 1-Ethyl-3-methyl-1*H*-imidazolium Tetrafluoroborate. *Helv. Chim. Acta* **87**, 2556 (2004).
27. Talaty, E. R., Raja, S., Storhaug, V. J., Dölle, A. & Carper, R. W. Raman and Infrared Spectra and ab Initio Calculations of C₂₋₄MIM Imidazolium Hexafluorophosphate Ionic Liquids. *J. Phys. Chem. B* **108**, 13177 (2004).
28. Köddermann, T., Wertz, C., Heintz, A. & Ludwig, R. Ion-Pair Formation in the Ionic Liquid 1-Ethyl-3-methylimidazolium Bis(triflyl)imide as a Function of Temperature and Concentration. *ChemPhysChem* **7**, 1944 (2006).
29. Bagno, A., D'Amico, F. & Saielli, G. Computer simulation of diffusion coefficients of the room-temperature ionic liquid [bmim][BF₄]: Problems with classical simulation techniques. *J. Molec. Liq.* **131-132**, 17 (2007).
30. Tsuzuki, S., Tokuda, H. & Mikami, M. Theoretical analysis of the hydrogen bond of imidazolium C₂-H with anions. *Phys. Chem. Chem. Phys.* **9**, 4780 (2007).

31. Adya, A. K. Nanoscopic structure of ionic liquids by neutron and X-ray diffraction. *J. Indian Chem. Soc.* **82**, 1197 (2005).
32. Hardacre, C., Holbrey, J. D., McMath, S. E. J., Bowron, D. T. & Soper, A. K. Structure of molten 1,3-dimethylimidazolium chloride using neutron diffraction. *J. Chem. Phys.* **118**, 273 (2003).
33. Hardacre, C., McMath, S. E. J., Nieuwenhuyzen, M., Bowron, D. T. & Soper, A. K. Liquid structure of 1,3-dimethylimidazolium salts. *J. Phys. C* **15**, S159 (2003).
34. Dymek, C. J., Jr., Grossie, D. A., Fratini, A. V. & Adams, W. W. Evidence for the Presence of Hydrogen-Bonded Ion-Ion Interactions in the Molten Salt Precursor, 1-methyl-3-ethylimidazolium chloride. *J. Mol. Struct.* **213**, 25 (1989).
35. Holbrey, J. D. *et al.* Crystal polymorphism in 1-butyl-3-methylimidazolium halides: supporting ionic liquid formation by inhibition of crystallization. *Chem. Comm.*, 1636 (2003).
36. Kölle, P. & Dronskowski, R. Hydrogen Bonding in the Crystal Structures of the Ionic Liquid Compounds Butyldimethylimidazolium Hydrogen Sulfate, Chloride, and Chloroferrate(II,III). *Inorg. Chem.* **43**, 2803 (2004).
37. Hayashi, S., Ozawa, R. & Hamaguchi, H. Raman Spectra, Crystal Polymorphism, and Structure of a Prototype Ionic-Liquid [bmim]Cl. *Chem. Lett.* **32**, 498 (2003).
38. Katayanagi, H., Hayashi, S., Hamaguchi, H. & Nishikawa, K. Structure of an ionic liquid, 1-*n*-butyl-3-methylimidazolium iodide, studied by wide-angle X-ray scattering and Raman spectroscopy. *Chem. Phys. Lett.* **392**, 460 (2004).
39. Nishikawa, K. *et al.* Melting and Freezing Behaviors of Prototype Ionic Liquids, 1-Butyl-3-methylimidazolium Bromide and Its Chloride, Studied by Using a Nano-Watt Differential Scanning Calorimeter. *J. Phys. Chem. B* **111**, 4894 (2007).
40. Huddleston, J. G. *et al.* Characterization and comparison of hydrophilic and hydrophobic room temperature ionic liquids incorporating the imidazolium cation. *Green Chem.* **3**, 156 (2001).
41. Ngo, H. L., LeCompte, K., Hargens, L. & McEwen, A. B. Thermal properties of imidazolium ionic liquids. *Therm. Acta* **357-358**, 97 (2000).
42. Ripmeester, J. A., Gordon, P., Enright, G. & Lang, S.
43. Chapman, R., P. & Bryce, D. L. A high-field solid-state ^{35/37}Cl NMR and quantum chemical investigation of the chlorine quadrupolar and chemical shift tensors in amino acid hydrochlorides. *Phys. Chem. Chem. Phys.* **9**, 6219 (2007).

44. Weeding, T. L. & Veeman, W. S. Characterisation of the structure of inorganic chloride salts with chlorine solid state NMR. *J. Chem. Soc. , Chem. Commun.*, 946 (1989).
45. Hayashi, S. & Hayamizu, K. *Bull. Chem. Soc. Jpn.* **63**, 913 (1990).
46. Sandland, T. O., Du, L. -, Stebbins, J. F. & Webster, J. D. Structure of Cl-containing silicate and aluminosilicate glasses: A ^{35}Cl MAS-NMR study. *Geochim. Cosmochim. Acta* **68**, 5059 (2004).
47. Wasylishen, R. E., Bryce, D. L. & Gee, M. High-Field Chlorine NMR Spectroscopy of Solid Organic Hydrochloride Salts: A Sensitive Probe of Hydrogen Bonding Environment. *J. Phys. Chem. A* **105**, 10413 (2001).
48. Bryce, D. L. & Sward, G. D. Solid-state NMR spectroscopy of the quadrupolar halogens: chlorine-35/37, bromine-79/81, and iodine-127. *Magn. Reson. Chem.* **44**, 409 (2006).
49. Widegren, J. A., Laesecke, A. & Magee, J. W. The effect of dissolved water on the viscosities of hydrophobic room-temperature ionic liquids. *Chem. Comm.*, 1610-1611, 1612 (2005).
50. Harris, R. K., Becker, E. D., Cabral de Menezes, S.M., Goodfellow, R. & Granger, P. *Pure Appl. Chem.* **73**, 1795 (2001).
51. Bryce, D. L., Aebi, D. & Adiga, S. EFGShield -- A program for parsing and summarizing the results of electric field gradient and nuclear magnetic shielding tensor calculations. *Can. J. Chem.* **85**, 496 (2007).

Chapter 8: Appendices

8.1 NMR pulse sequence programs

zg; single-pulse:

```
;zg
;avance-version (02/05/31)
;1D sequence
```

```
#include <Avance.incl>
```

```
1 ze
2 30m
d1
p1 ph1
go=2 ph31
30m mc #0 to 2 F0(zd)
exit
```

```
ph1=0 2 2 0 1 3 3 1
ph31=0 2 2 0 1 3 3 1
```

```
;p11 : f1 channel - power level for pulse (default)
;p1 : f1 channel - high power pulse
;d1 : relaxation delay; 1-5 * T1
;NS: 1 * n, total number of scans: NS * TD0
```

```
;$Id: zg,v 1.7 2002/06/12 09:05:19 ber Exp $
```

zg; single pulse with high-power proton decoupling:

```
;hpdec
;avance-version (02/05/31)
;single pulse excitation with high power proton decoupling
;for use with high power X-amplifier
```

```
; !!! recable 1H channel f2 direct to probehead !!!
; !!! do not connect via the proton preamplifier !!!
```

```
#include <Avance.incl>
```

```
1 ze
2 30m do:f2
d1
```

```

10u p1:f1 p112:f2
(p1 ph1):f1
2u cw:f2
go=2 ph31
30m do:f2 mc #0 to 2 F0(zd)
exit

```

```

ph1=0 2 1 3
ph31=0 2 1 3

```

```

;p11 : f1 channel - power level for pulse (default)
;          [about 0.0 for B-LAX 300]
;p112: f2 channel - power level for CW decoupling
;          [about -3.0 for B-LAH 100]
;p1 : f1 channel - 90 degree high power pulse
;p15: f1(f2) channel - contact pulse
;d1 : relaxation delay: 5 sec
;          (for Adamantane and Glycine set-up sufficient)
;NS: 4 * n, total number of scans: NS * TD0
;DS: 0

```

;aq: adjust to maximum 50 msec, td ca 2k.

;\$Id: hpdec,v 1.7 2002/06/12 09:04:49 ber Exp \$

90/180 echo:

```

;echo
;avance-version (02/05/31)
;1D sequence

```

```

;d1 : relaxation delay
;p1 : 90 deg pulse
;p2 : 180 deg pulse
;p11 : power level (F1)
;cnst31: spinning frequency (in Hz)
;l31 : no. rotor periods in echo
;d6 : first echo delay
;d7 : second echo delay

```

```
#include <Avance.incl>
```

```

"d6 = (1.0s/cnst31)*l31 - p1/2 - p2/2"
"d7 = (1.0s/cnst31)*l31 - p1/2 - p2/2 - de"

```

```

1 ze
2 30m
d1
p1 ph1
d6

```

```

p2 ph2
d7
go=2 ph31
30m mc #0 to 2 F0(zd)
exit

```

```

ph1=0 1 2 3
ph2=0 0 0 0 1 1 1 1 2 2 2 2 3 3 3 3
ph31=0 3 2 1 2 1 0 3

```

90/180 echo with high power proton decoupling:

```

;
;sssecho for dsx-400 (AQR)
;solid state echo: A.C.Kunwar, G.L.Turner, E. Oldfield, JMR 69 (1986) 124-127
;ILM 27/9/1997
;90-180 solid echo sequence for wide line observation with the phase cycle
;suitable for quadrupole nuclei
;
;*****
;
;use selective 90-degree pulse for quadrupole nuclei
;p1 : 90-degree excitation pulse
;p3 : 180 inversion pulse
;p11 : power for excitation pulse
;p12 : power for inversion pulse

#include <Avance.incl>

1 ze
2 d1 p11:f1 p12:f2
   (p1 ph1):f1
   d6 p12:f1
   (p3 ph2):f1
   d7 cw:f2
   1u:f1 ph0:r ; reset DDS to reference phase, set phcor 0 for
               ; all signal in one channel
   1u adc ph31 ;start adc with ph31 channel routing
   aq          ;acquire data
2m
rcyc=2
wr #0
exit

ph0=0
ph10= 0 0 0 0 1 1 1 1 2 2 2 2 3 3 3 3
ph1 = 0 0 0 0 1 1 1 1 2 2 2 2 3 3 3 3
ph2 = 0 1 2 3
ph31= 3 1 3 1 2 0 2 0 1 3 1 3 0 2 0 2

;p1 : pi/2 pulse
;p3 : pi pulse
;d6 : delay between the pulses

```

```
;d7 : echo delay
```

T1 experiments: t1ir

```
;t1ir
;avance-version (00/02/07)
;T1 measurement using inversion recovery
```

```
#include <Avance.incl>
```

```
"p2=p1*2"
```

```
"d11=30m"
```

```
1 ze
2 d1
  p2 ph1
  vd
  p1 ph2
  go=2 ph31
  d11 wr #0 if #0 ivd
  lo to 1 times td1
exit
```

```
ph1=0 2
ph2=0 0 2 2 1 1 3 3
ph31=0 0 2 2 1 1 3 3
```

```
;p11 : f1 channel - power level for pulse (default)
;p1 : f1 channel - 90 degree high power pulse
;p2 : f1 channel - 180 degree high power pulse
;d1 : relaxation delay; 1-5 * T1
;d11: delay for disk I/O [30 msec]
;vd : variable delay, taken from vd-list
;NS: 8 * n
;DS: 4
;td1: number of experiments = number of delays in vd-list
```

```
;define VDLIST
```

```
;this pulse program produces a ser-file (PARMOD = 2D)
```

```
;$Id: t1ir,v 1.8 2002/06/12 09:05:15 ber Exp $
```

T2 experiments: t2_hahn

```
;t2 hahn echo
;19 March 2001, ILM
```

```

;avance-version
;T2 measurement using Hahn echo

#include <Avance.incl>

;;"p2=p1*2"
;;"d11=30m"

1 ze
2 d1
  p1 ph1
  vd
  p2 ph2
  vd
  go=2 ph31
  d11 wr #0 if #0 ivd
  lo to 1 times l4
exit

ph1=0 0 2 2 1 1 3 3
ph2=1 3 1 3 0 2 0 2
ph31=0 0 2 2 1 1 3 3

;p11 : f1 channel - power level for pulse (default)
;p1 : f1 channel - 90 degree pulse
;p2 : f1 channel - 180 degree pulse
;d1 : relaxation delay; 1-5 * T1
;d11: delay for disk I/O [30 msec]
;vd : variable delay, taken from vd-list
;L4: l4 = number of experiments = number of delays in vd-list
;NS: 8 * n
;DS: 4
;tdl: number of experiments

;define VDLIST

;this pulse program produces a ser-file (PARMOD = 2D)

```

8.2 Relaxation Time Experimental Data

The following tables contain data collected from T_1 and T_2 experiments on emim, bmim, bdmim [Cl] and emim and bmim[Br], used for the plots in Figure 34 and Figure 35 respectively. The cells labelled “ave. std. dev.” refer to the average of the standard

deviations of each T_1 and T_2 measurement, which is a mathematical fit to the theoretical inversion recovery curve discussed in Section 2.3.5. For each curve, sixteen spectra were collected and analyzed.

emim-Cl						emim-Br					
Temp (K)	1/T	T1 (ms)	T2 (ms)	T1/T2	% s.d.	Temp (K)	1/T	T1 (ms)	T2 (ms)	T1/T2	% s.d.
363	0.0028	3.16	1.69	1.87	5.550	383	0.0026	108.56	89.14	1.22	7.907
353	0.0028	2.15	1.14	1.89	4.805	378	0.0026	116.73	99.66	1.17	15.69
343	0.0029	26.00	0.26	100.00	18.56	373	0.0027	86.79	79.46	1.09	13.86
						368	0.0027	83.00	51.94	1.60	9.404
						363	0.0028	66.16	50.90	1.30	11.40
						358	0.0028	46.29	38.68	1.20	5.947

bmim-Cl						bmim-Br					
Temp (K)	1/T	T1 (us)	T2 (us)	T1/T2	% s.d.	Temp (K)	1/T	T1 (ms)	T2 (ms)	T1/T2	% s.d.
343	0.0029	394.68	165.91	2.38	3.474	383	0.0026	25.32	27.49	0.92	8.476
338	0.0030	321.86	112.53	2.86	3.699	378	0.0026	19.53	16.63	1.17	7.163
333	0.0030	270.84	94.69	2.86	3.872	373	0.0027	18.16	16.40	1.11	8.315
328	0.0030	256.04	106.72	2.40	7.705						

bdmim-Cl					
Temp (K)	1/T	T1 (us)	T2 (us)	T1/T2	% s.d.
378	0.0026	505.28	239.49	2.11	4.304
373	0.0027	398.46	149.45	2.67	3.644
368	0.0027	368.12	116.20	3.17	3.651
363	0.0028	315.13	108.84	2.90	6.062
358	0.0028	302.46	79.51	3.80	3.959

8.3 NMR Acquisition Parameters

Table 7 ^{35}Cl SSNMR MAS acquisition parameters (21.15 T)

	all samples
$\pi/2$ pulse (μs)	3.1
acq. time (μs)	20.53
recycle delay (s)	2
number of scans	1k
sweep width (kHz)	50
spin rate (kHz)	10

Table 8 ^{35}Cl SSNMR static acquisition parameters

	emim		bmim		bdmim		mbpyr	
	9.4 T	21.15 T						
$\pi/2$ pulse (μs)	2.1	3.1	2.1	3.1	2.1	3.1	2.1	3.1
acq. time (ms)	10	10	10	5.17	10	10.29	10	10.29
recycle delay (s)	1	1	1	1	1	1	1	1
echo delay (μs)	40	-	40	-	40	-	40	-
number of scans	1500	2k	1500	2k	12k	4k	1500	4k
sweep width (kHz)	50	50	50	100	50	50	50	50

Table 9 ³⁵Cl liquid NMR acquisition parameters

	all samples
$\pi/2$ pulse (μ s)	9
acq. time (ms)	25.7
recycle delay (s)	2
number of scans	5k
sweep width (kHz)	20

Table 10 ⁷⁹Br SSNMR static acquisition parameters

	emim		bmim		dmpyrro		bNH ₃	
	11.75 T	21.15 T	11.75 T	21.15 T	9.4 T	21.15 T	11.75 T	21.15 T
$\pi/2$ pulse (μ s)	1.4	2.1	1.4	3.5	1.88	2.1	1.9	1.4
acq. time (μ s)	200	560	350	560	700	560	350	300
recycle delay (s)	1	1	1	1	5	1	1	1
echo delay (μ s)	700	20	50	20	-	20	20	20
number of scans	60k	4k	4k	4k	30k	1k	57k	2k
sweep width (MHz)	0.36	1	0.36	1	1.5	1	0.36	1

Table 11 ⁷⁹Br liquid NMR acquisition parameters

	emim	bmim
$\pi/2$ pulse (μ s)	3.9	3.9
acq. time (ms)	2.56	2.56
recycle delay (s)	2	2
number of scans	2k	2k
sweep width (kHz)	40	100

Table 12 ¹²⁷I SSNMR static acquisition parameters

	tmim		dmpyrro		bdmim	
	21.15 T	11.75 T	11.75 T	21.15 T	11.75 T	21.15 T
$\pi/2$ pulse (μ s)	1	1	4.2	1	1.6	1.6
acq. time (μ s)	300	720	560	350	560	560
recycle delay (s)	1	1	1	1	1	1
echo delay (μ s)	20	200	20	50	20	20
number of scans	50k	70k	10k	60k	16k	16k
sweep width (MHz)	1	1	1	1	0.5	0.5

Table 13 ¹²⁷I SSNMR MAS acquisition parameters

	dmpyrro	bdmim
$\pi/2$ pulse (μ s)	6	3.1
acq. time	1.33 ms	690 μ s
recycle delay (s)	1	1
number of scans	1k	16k
sweep width (kHz)	400	400
spin rate (kHz)	30	35

8.4 Gaussian 98 Input Files

This section contains representative examples of input files used for theoretical calculations executed by Gaussian 98. For brevity's sake, full atomic coordinates have been excluded (and other abbreviations which will be so noted in brackets). The general form of all input files were identical for a given calculation; a single example has been chosen from each group of calculations.

Rough Proton Optimization Example

```
%mem=245Mw
#P HF/STO-3G Nosymm Opt=ModRedundant maxdisk=2000Mb

MBPyr-Cl Cl#1 rough optimization of H atoms

7 1
Cl  0.001  3.048  6.558
C   1.658  0.745  3.164
N   -5.498  -0.04  3.099
H   0.936  1.259  2.88
(full coordinate list deleted)

* K
* * K
* * * K
* * * * K
* B
* F
74 A (refers to "unfreezing" proton designated number 74; all
subsequent such commands for remaining protons deleted)
```

Refined Proton Optimization Example

```
%mem=245Mw  
#P B3LYP/3-21G* Opt=ModRedundant maxdisk=2000Mb
```

```
BMMIM-C1 optimizing protons
```

```
4 1  
(atomic coordinates deleted, as above)
```

```
* * K  
* * * K  
* * * * K  
* B  
* F  
43 A  
(remaining commands deleted, as above)
```

EFG Calculation Example

```
%mem=245Mw  
#P HF Gen Int=FineGrid NMR=GIAO IOP(10/75=2) maxdisk=2000Mb
```

```
BDMIM-C1 EFG calculation
```

```
4 1  
(atomic coordinates deleted, as above)
```

```
C1 0  
cc-pVTZ  
****  
H C N 0  
cc-pVDZ  
****
```

Shielding Calculation Example

```
%mem=245Mw
```

```
#P B3LYP Gen Int=FineGrid NMR=GIAO IOP(10/75=2) maxdisk=2000Mb
```

```
EMIM-Cl(1) shielding calculation
```

```
8 1
```

```
(atomic coordinates deleted, as above)
```

```
Cl 0
```

```
aug-cc-pVDZ
```

```
****
```

```
H C N 0
```

```
cc-pVDZ
```

```
****
```